



Dynamics of magma mixing and magma mobilisation beneath Mauna Loa—insights from the 1950 AD Southwest Rift Zone eruption

Maren Kahl¹ · Daniel J. Morgan² · Carl Thornber³ · Richard Walshaw² · Kendra J. Lynn⁴ · Frank A. Trusdell⁴

Received: 8 April 2023 / Accepted: 11 October 2023 / Published online: 29 November 2023
© The Author(s) 2023

Abstract

Eruptions from Mauna Loa's Southwest Rift Zone (SWRZ) pose a significant threat to nearby communities due to high eruption rates and steep slopes resulting in little time for evacuation. Despite the large body of research done on Mauna Loa, knowledge of the timing and duration of magma residence and transfer through its internal plumbing system is still poorly constrained. This study presents a first quantitative look at thermochemical conditions and timescales of potentially deep storage and disaggregation of magmatic mush during the run-up to the voluminous 1950 AD SWRZ eruption. Details of heterogeneous compositions and textures of the macrocryst and glomerocryst cargo in 1950 AD lavas suggest magma mixing and crystal recycling along the entire plumbing system. Furthermore, the crystal cargo contains evidence for the direct interaction between primitive, deeply stored magma and pockets of more evolved magma stored at shallow to intermediate depths. An enigmatic attribute of 1950 near-vent lava is the near-ubiquitous presence of subhedral, unreacted Mg-rich orthopyroxene phenocrysts ($Mg\# > 80$). Phase relations of Mauna Loa olivine-tholeiite indicate that orthopyroxene joins olivine as a primary phase at pressures higher than 0.6 GPa. Coexisting Mg-rich olivine and orthopyroxene and the occurrence of harzburgitic (olivine-orthopyroxene) glomerocrysts provide evidence for cognate crystallisation at near-Moho (~ 18 km) depths (Thornber and Trusdell 2008). Petrogenetically diverse populations of glomerocrysts and macrocrysts alongside evidence of multilevel magma storage indicate a network of ephemeral and possibly interconnected magma pockets from near-Moho depths to the upper/mid-crust. Fe-Mg diffusion chronometry applied to 1950 AD olivine populations implies rapid mobilisation and transport of large volumes of magma ($376 \times 10^6 \text{ m}^3$) from near-Moho storage to the surface within less than 8 months, with little residence time (~ 2 weeks) in the shallow (3–5 km) plumbing system.

Keywords Mauna Loa · 1950 AD eruption · Olivine · Diffusion chronometry · Magma mixing · Hawai'i

Introduction

Repeated signals of volcanic unrest in the form of increasing seismicity and long-term inflation lasting from 2003 until the recent eruption episode between November and December 2022, have fuelled speculation that Mauna Loa could enter a renewed phase of eruptive activity (e.g. La Marra et al. 2015). With 34 eruptions since 1832 (Lockwood and Lipman 1987), averaging one eruption every 5.26 years, Mauna Loa is not only the largest and most voluminous (~ 80,000 km³, e.g. Garcia et al. 1995; Lipman 1995) but also one of the Earth's most active volcanoes (Trusdell 2012). Its eruptive activity is characterised by summit and flank eruptions. Summit eruptions are constrained to the oval-shaped summit caldera Moku'āweoweo, whereas rift zone eruptions usually commence with summit activity,

Editorial responsibility: A. V. Ivanov

✉ Maren Kahl
Maren.Kahl@geow.uni-heidelberg.de

- ¹ Institut für Geowissenschaften, Universität Heidelberg, Im Neuenheimer Feld 234-236, 69120 Heidelberg, Germany
- ² School of Earth and Environment, The University of Leeds, Leeds LS2 9JT, UK
- ³ U.S. Geological Survey, Cascade Volcano Observatory, 1300 SE Cardinal Court, Vancouver, WA 98683, USA
- ⁴ U.S. Geological Survey, Hawaiian Volcano Observatory, 1266 Kamehameha Avenue, Hilo, HI 96721, USA

but terminate with more voluminous eruptions along either of its two rift zones (e.g. Lockwood and Lipman 1987; Rhodes 1995; Trusdell 2012). The Northeast Rift Zone (NERZ) extends east-northeast from the summit caldera for about 40 km (Fig. 1a), before it becomes progressively wider and more diffuse and is buried by younger Kīlauea lavas (Rhodes 1995). Since 1843, the NERZ has been the eruptive locus for 26% of the eruptions (e.g. Trusdell 1995). The Southwest Rift Zone (SWRZ) is the longer of the two rift zones, its sub-areal part stretches over 70 km in length and extends

much further below sea level, and it has been the source for 25% of the eruptions (Lockwood and Lipman 1987; Rhodes 1995; Trusdell 1995). High effusion rates (~9.6 km/h, Honukua flow of the 1950 SWRZ eruption; Finch and Macdonald 1953) combined with steep slopes (>15° degree) result in fast moving lava flows, and the close proximity of developed areas (e.g. South Kona, Ka'ū) leave little time for evacuations, ultimately presenting a major threat to communities and settlements in the event of an eruption emerging from Mauna Loa's SWRZ (Trusdell 1995, 2012).

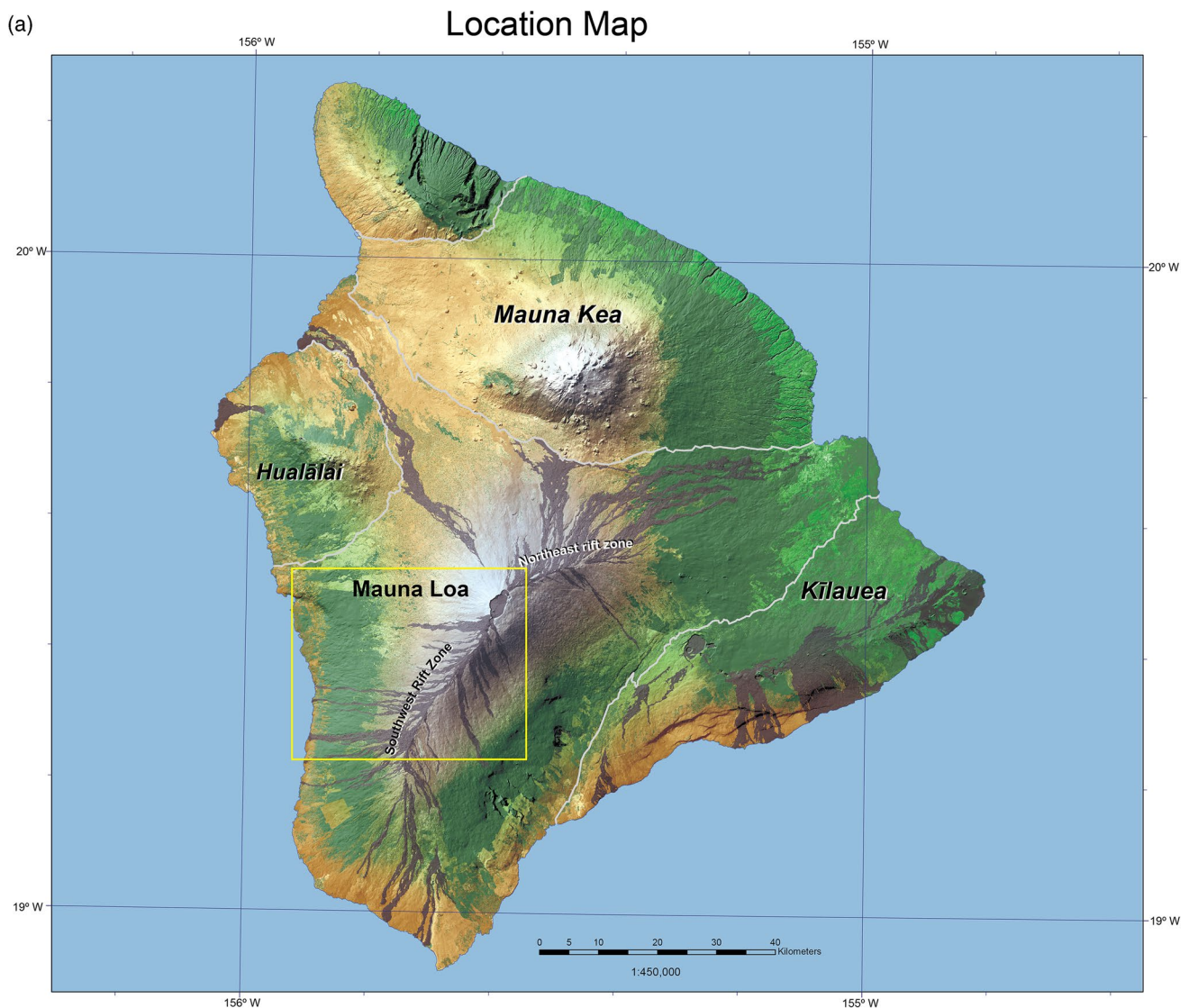


Fig. 1 **a** Google Earth overview image of the island of Hawai'i showing the location of Mauna Loa and its two rift zones: SWRZ, Southwest Rift Zone; NERZ, Northeast Rift Zone (figure modified from Couperthwaite et al. 2022). Yellow rectangle showing the location of the 1950 AD eruption site along the SWRZ. **b** Map displaying the 1950 AD lava flow field and the eruptive fissure system that opened along the SWRZ of Mauna Loa. Filled triangles: sample locations of

the nine near-vent 1950 AD samples considered in this study. A–G: 1950 AD lava flows. A: Upper rift flow; B: upper flank flow; C: Honukua flow; D: Ka'ōhe flow; E: Punalu'u flow; F: Ka'apuna flow; G: Kahuku flow. 1: First fissure segment that opened between ~3,658 m and 3,353 m a.s.l. 2: Second fissure segment that unzipped between 3,200 and 2,590 m a.s.l. Figure redrawn from Finch and Macdonald (1953).

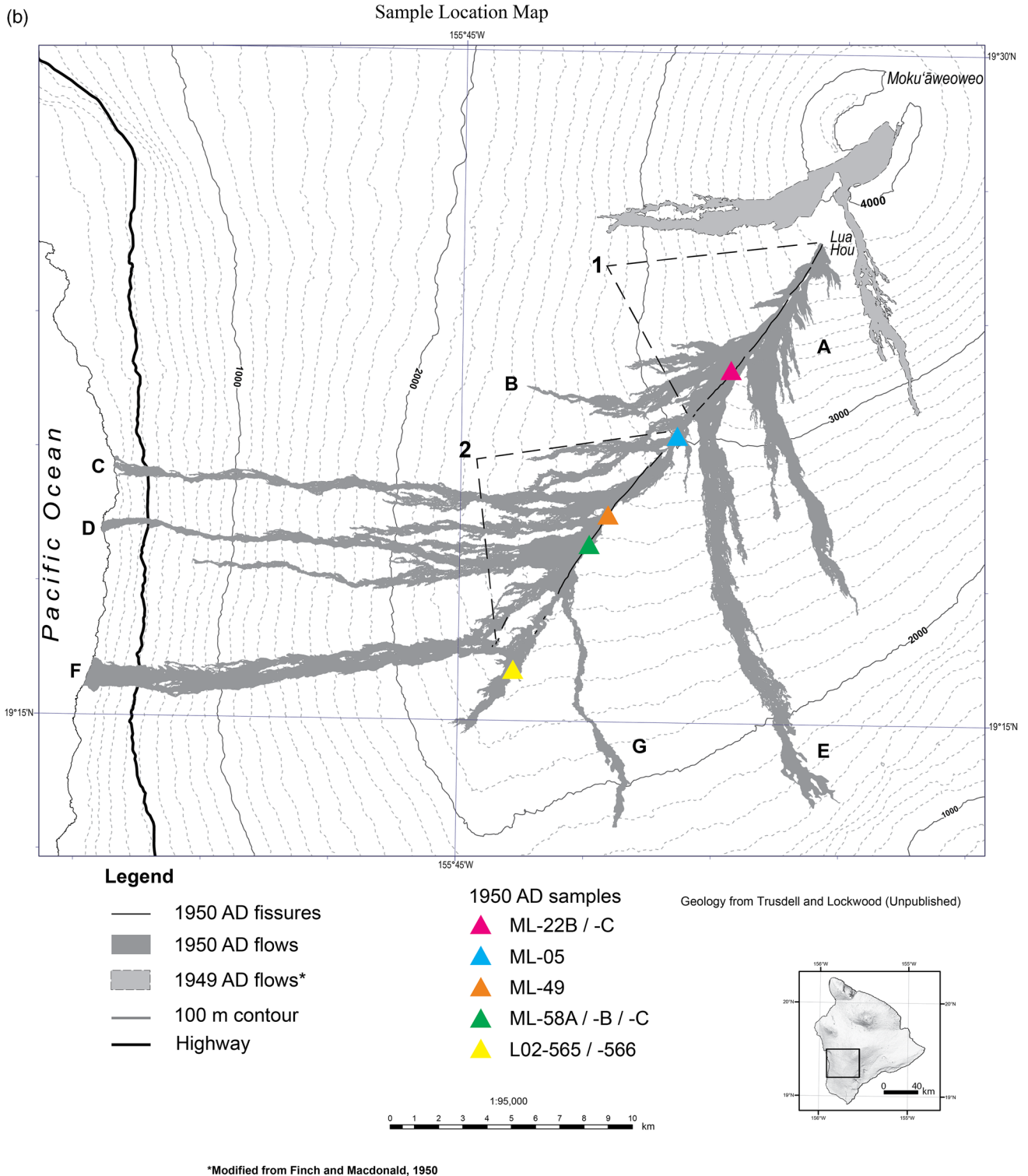


Fig. 1 (continued)

The 1950 AD eruption and its precursors

The 1950 AD eruption ranks as one of the largest at Hawai‘i of the past 200 years (Lockwood and Lipman 1987). During

a 23-day period in June 1950, a total volume of $376 \times 10^6 \text{ m}^3$ of lava (>70% erupted during the first 2 days) erupted from an ~ 18-km-long series of fissures extending from ~ 3,658 down to 2,590 m a.s.l. elevation along the SWRZ

(Lockwood and Lipman 1987; Finch and Macdonald 1953). The 1950 AD eruption was preceded by three eruptions in 1940 AD (summit), 1942 AD (NERZ), and 1949 AD (summit). For several months after the 1949 AD summit eruption, a lack of westward tilt on Kīlauea's summit was suggestive of continued magmatic pressurisation of the Mauna Loa edifice (Finch and Macdonald 1953). In March 1950, inflation of Mauna Loa was recorded by eastward tilting at Kīlauea (Finch and Macdonald 1953). The eruption onset was heralded by seismic swarms beginning on March 25 and becoming more frequent in the days and hours before the onset of eruptive activity (June 1), culminating in a magnitude 6.4 earthquake on May 29 beneath Mauna Loa's west flank (Wyss and Koyanagi 1992; Finch and Macdonald 1953). On the night of June 1, 1950, eruptive fissures opened along the summit and uppermost SWRZ (Fig. 1b) of Mauna Loa (Finch and Macdonald 1953). The first 2.4-km-long fissure segment (indicated as 1 in Fig. 1b) opened between ~ 3,658 m and 3,353 m a.s.l. and gave rise to minor lava effusions that ceased after a few hours. The second fissure segment (indicated as 2 in Fig. 1b) unzipped that same night between 3,200 and 2,590 m a.s.l. Eruptive activity along the upper portion of the second fissure segment lasted for about a week, whereas the lower sections remained active for 3 weeks (Finch and Macdonald 1953). On June 23, the eruptive activity ceased and a compound lava flow field covering a total area of 112 km² had formed (Lockwood and Lipman 1987). A total of seven lava flows advanced downslope, three to the southeast and four to the west (Finch and Macdonald 1953). The combination of steep slopes and high lava output rates (maximum 1000 m³/s; average >350 m³/s; Kauahikaua et al. 2003) enabled some of the 1950 lava flows to reach maximum speeds of up to 3–4 m/s while propagating downslope towards the ocean (Finch and Macdonald 1953). Flows originating from lower elevation fissures made it to the South Kona coast in as little as 3 h (Trusdell 1995), endangering lives, destroying property, and severing essential infrastructure.

This study

Despite the large body of research done on Mauna Loa, knowledge of the timing and duration of magma transfer and residence throughout its internal plumbing system is limited (Couperthwaite et al. 2020; Couperthwaite et al. 2022). In this study, we use a quantitative petrological approach that links major and minor element geochemistry of mineral (mainly olivine) and melt phases (groundmass glass and melt inclusions) with geothermometry and diffusion modelling to constrain pre-eruptive magma storage conditions and time-scales of deep mush disintegration and mobilisation in the run-up towards the 1950 AD eruption. We approach this by studying a suite ($n=9$) of near-vent, lava ($n=6$), and spatter

($n=3$) samples that were erupted from vents that opened progressively between ~ 3,660 and 2,590 m during the first 24 h of the eruption (Fig. 1b). Petrologic details of these samples are evaluated within the context of bulk rock and glass major element chemistry of over 100 samples collected along the entire extent of fissure vents. The entire 1950 AD suite is listed along with location, lithologic type, and vent elevation in Supplementary Data table S1. In this contribution, we start with a brief description of petrography, mineral, glass (groundmass, melt inclusions), and whole rock chemistry, followed by a brief summary of olivine zoning types and olivine-melt equilibria. We then apply mineral-melt thermometry to constrain T conditions of magma storage and use this information to provide context for Fe-Mg olivine diffusion chronometry to develop a conceptual model of the magmatic events that lead to the 1950 AD eruption.

Methods

Major and minor elements were analysed in 45 groundmass glasses ($n=422$ spot analysis), 20 olivine-hosted melt inclusion glasses ($n=28$ spot analysis), 183 olivine, 31 orthopyroxene, 6 clinopyroxene, 20 plagioclase, and 40 spinel crystals by electron microprobe analysis using the JEOL JXA 8230 instrument at the University of Leeds Microscopy and Spectroscopy Centre (olivine and pyroxene analysis), the JEOL 8230 SuperProbe instrument at the University of Iceland (melt inclusion glass and spinel analysis), JEOL 8900 instrument at the USGS Denver Microbeam Facility (groundmass glass analysis), and the JEOL SuperProbe JXA-iSP100 instrument at the electron microscopy lab for Geomaterials at Heidelberg University (plagioclase analysis). We used an accelerating voltage of 15 kV; beam currents of 10 nA (plagioclase, melt inclusion glasses), 20 nA (groundmass glasses and spinel), and 30 nA (olivine, ortho- and clinopyroxene); and beam spot sizes ranging from fully focussed (olivine, spinel, ortho- and clinopyroxene) to a diameter of 5 μm (plagioclase), 10 μm (melt inclusions), and 10–20 μm (groundmass glasses). A list of primary standards used for calibration, including peak and background count times, is provided in the Supplementary Material table 1. Precision was assessed using EPMA software-calculated 1 sigma count statistic errors (Wieser et al. 2022) and repeat analysis of the VG-A99 basalt glass standard (see Supplementary Material). Accuracy was monitored by measuring the following secondary standards during each session: plagioclase (anorthite) from Great Sitkin Island, Alaska (NMNH137041); GEO2 MKII olivine; GEO2 MKII diopside; and basalt glass VG-A99 (USNM 113498-1; Makaopuhi Lava Lake). Precision and accuracy estimates are provided in the Supplementary Material.

Concentrations of major elements in whole rocks were measured at the USGS Denver XRF Laboratory using wavelength-dispersive spectrometry X-ray fluorescence techniques described by Taggart et al. (1987). Samples were crushed using a ceramic alumina rocker and platen and powdered in an alumina shatterbox (e.g. Thornber et al. 2002). Repeated XRF analyses of the two USGS Kīlauea whole-rock standards BHVO-1 and BHVO-2 were performed as analytical control. Standard reproducibilities (at 1 sigma error) are 0.007 wt% for K₂O, 0.0003 wt% for MnO, 0.02 wt% for TiO₂ and P₂O₅, 0.008 wt% for CaO, 0.1 wt% for Na₂O, 0.06 wt% for Al₂O₃, 0.08 wt% for Fe₂O₃* (total-iron), 0.06 wt% for MgO, and 0.1 wt% for SiO₂.

Diffusive anisotropy in olivine was corrected for by characterizing the orientation of the crystallographic *a*-, *b*-, and *c*-directions in olivine using electron backscatter diffraction (EBSD) mapping (Costa and Chakraborty 2004; Prior et al. 1999) on the FEI Quanta 650 FEGSEM at the University of Leeds Electron Microscopy and Spectroscopy Centre (LEMAS). EBSD data were acquired using an accelerating voltage of 20.0 kV, a working distance of 27.2 mm, a specimen tilt of 69.8°, and a detector insertion distance of 207 mm (Kahl et al. 2017). Details on EBSD analysis are available in the Supplementary Material.

All melt inclusion (MI) compositions (*n*=28) were corrected for post-entrapment crystallisation (PEC) that took place during natural quenching. Details on PEC correction are available in the Supplementary Material and Fig. S1.

Petrography

In this study we focus on nine near-vent samples that were erupted from mid- to lower elevation vents (3,292 to 2,347 m; Fig. 1b) representing basaltic lava flow or spatter samples (see Supplementary Data table S1) with porphyritic (porphyritic index ~ 5–30%) and scoriaceous textures containing ubiquitous macrocrysts of olivine, orthopyroxene, clinopyroxene, and rare plagioclase, embedded in a fine-grained, glassy to hypocrySTALLINE, intersertal groundmass. The term macrocryst is used to refer to crystals with a minimum long axis length of >0.5 mm (e.g. Thomson and Maclennan 2013), without genetic implications. The groundmass usually consists of microlites of plagioclase, clinopyroxene, occasionally olivine, and minor spinel. Samples that erupted from higher vent elevations (>3,400 m) are plagioclase- and clinopyroxene-phyric with rare orthopyroxene and disaggregated glomerophyric gabbro and rare gabbro-norite clusters (Thornber and Trusdell 2008). Samples from higher vent elevations are olivine poor (Finch and Macdonald 1953) and will not be discussed in this study. The following descriptions refer to mineral phases contained in mid- to lower elevation vent samples.

Olivine (Fo_{70–89}; table S2) is mostly sub- or anhedral with crystal sizes ranging between 0.2 and 2.3 mm (long axis). Normal and complex reverse zoning, inclusions of spinel (mostly Cr-rich spinel), and partially re-crystallised MIs are common. Rims are usually anhedral and strongly embayed or rounded with occasional dendritic or hopper morphologies. Olivine-orthopyroxene-clinopyroxene-plagioclase glomerocrysts are also observed (Fig. S2).

Orthopyroxene (Wo₅, En_{68–79}, Fs_{15–27}, and Mg#_{69–86}; table S3) forms euhedral to subhedral crystals with sizes between 0.2 and 2.1 mm (long axis). Besides weak oscillatory and sector zoning, orthopyroxenes display pronounced normal, reverse, and complex zoning, the latter with normally zoned cores and reverse zoning towards the outermost rims. Reversely zoned orthopyroxenes often contain anhedral, resorbed low-Mg cores overgrown by Mg-rich rims. Rims of normal, reverse, and complexly zoned orthopyroxenes are eu- to subhedral and occasionally overgrown by clinopyroxene. Orthopyroxene forms glomerocrysts or cognate xenoliths with clinopyroxene, plagioclase, olivine, and other orthopyroxenes (Fig. S3).

Clinopyroxene (Wo_{26–40}, En_{46–60}, Fs_{9–18}, and Mg#_{73–86}; table S3) forms sub- to anhedral crystals with sizes between 0.3 and 2.3 mm (long axis). Besides oscillatory and sector zoning, clinopyroxene crystals also display reverse zoning with corroded low-Mg cores overgrown by Mg-rich rims. Rims are often sub- to anhedral, occasionally oscillatory zoned and may contain plagioclase microlites from the surrounding groundmass. Clinopyroxene occasionally forms glomerophyric clusters with orthopyroxene, plagioclase, and olivine (Fig. S4).

Plagioclase (An_{59–82}; table S4) forms eu- to subhedral crystals of 0.2–1.2 mm (long axis). Besides oscillatory zoning, plagioclase displays weak normal and reverse zoning. Rims are often eu- to subhedral. Plagioclase rarely occurs as macrocrysts but usually forms glomerophyric clusters with orthopyroxene and clinopyroxene (Fig. S5).

Chromium-spinel (Mg#_{41–60}; Cr#_{57–70}; table S5) forms euhedral to anhedral crystals of variable size (0.03 to <0.3 mm) that commonly occur as inclusions in olivine. Spinel also occurs in the groundmass and in interstices between adjacent olivine macrocrysts in glomerocrysts. As inclusions in olivine, spinel crystals are usually euhedral to subhedral.

Mineral, glass, and whole-rock compositions

Glass and whole-rock compositions

Groundmass glass and PEC-corrected melt inclusion compositions along with whole-rock compositions are depicted in Fig. 2 and in figure S6 (all glass and whole-rock data are provided in tables S6–S8). Glass and whole-rock compositions

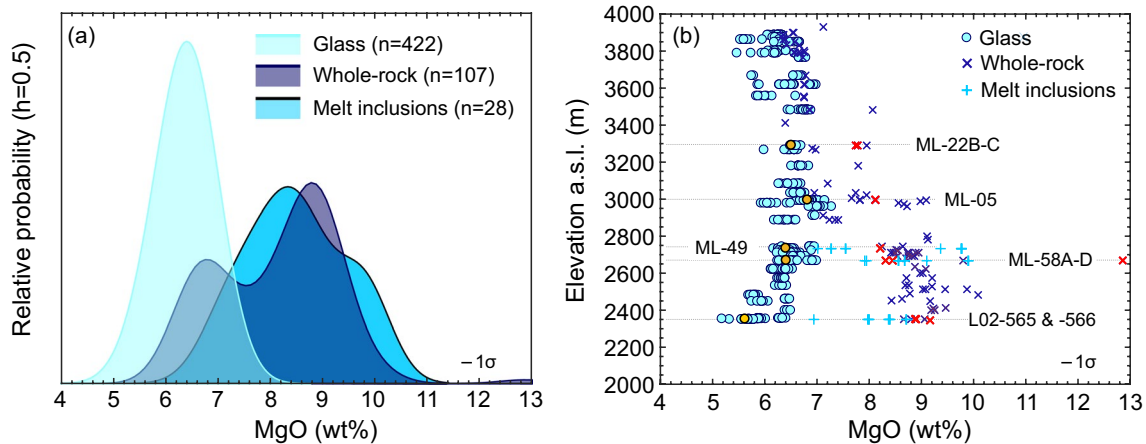


Fig. 2 **a** Kernel density estimates (KDEs) illustrating MgO contents of groundmass glasses, PEC-corrected melt inclusions, and whole rocks of the 1950 AD eruption of Mauna Loa. **b** MgO content of

eruption products versus vent elevation. Yellow-filled circles and red crosses: average glass and whole rock data of samples studied in more detail in this study. Error bars, 1σ

from the entire 1950 AD sample suite show well-defined peaks in kernel density estimate (KDE) plots illustrating the distribution of the MgO content (Fig. 2a). Groundmass glass compositions have MgO contents within the range 5.1–7.2 wt% ($\text{Mg\#}_{\text{liquid}}$ 47.1–62.3) with a mean of 6.3 wt% (mean $\text{Mg\#}_{\text{liquid}}$ 54.5). Whole-rock compositions display a larger compositional variability with MgO contents ranging between 6.3 and 12.8 wt% MgO. PEC-corrected olivine-hosted (Fo_{82-89}) melt inclusions from lower-vent elevations (2,736–2,353 m; Fig. 2b) are more variable than groundmass glasses and plot at comparatively higher MgO, between 7.0 and 10.0 wt% (mean 8.6 wt%), with $\text{Mg\#}_{\text{liquid}}$ 59–70.4.

Figure 2b illustrates the variability of the MgO content in the analysed glasses and whole rocks as a function of eruption vent elevation (metres a.s.l.). Glass and whole-rock compositions that erupted from vents higher than $\sim 3,400$ m partly overlap, with MgO contents between 5.4 and 6.9 wt% ($\text{Mg\#}_{\text{liquid}}$ 48.7–57.4). Chemically evolved, low-MgO and low-Fo olivine material that erupted from vents $> 3,400$ m represents a low-pressure fractionated magma component consistent with shallow residual magma remnant of the 1949 AD summit eruptions or earlier shallow intrusions (Thornber and Trusdell 2008).

MgO contents of glasses and whole rocks from vents $< 3,400$ m become widely decoupled. Whole-rock compositions become more magnesian (6.4–12.9 wt% MgO) with decreasing vent elevation. Groundmass glass compositions are also more Mg-rich, reaching maximum MgO contents of 7.3 wt% ($\text{Mg\#}_{\text{liquid}}$ 58.5) at an elevation of $\sim 2,963$ m, before becoming again less magnesian at lower elevations.

Variability diagrams summarised in figure S6 show that despite large differences in their MgO contents, the glasses and whole rocks of the 1950 AD eruption have very similar and overlapping SiO_2 (50.6–55.0 wt%), TiO_2 (0.9–2.7

wt%), CaO (9.2–11.2 wt%), Al_2O_3 (12.3–15.2 wt%), and K_2O (0.2–0.6 wt%) contents.

Samples studied in detail were erupted from vent elevations $< 3,400$ m (Fig. 2b; yellow-filled circles and red crosses) with whole-rock and glass MgO contents ranging between 5.6 and 12.9 wt%.

Olivine

Kernel density estimates (KDEs) showing forsterite distributions of 183 olivine core and rim compositions from 9 near-vent samples that erupted from elevations $< 3,400$ m during the eruption are illustrated in Fig. 3. In the following, we describe how olivine core and rim compositions vary with vent elevation. KDE diagrams illustrating forsterite distributions are arranged according to decreasing vent elevations, beginning with olivines that were erupted from the highest elevations (Fig. 3 a–f).

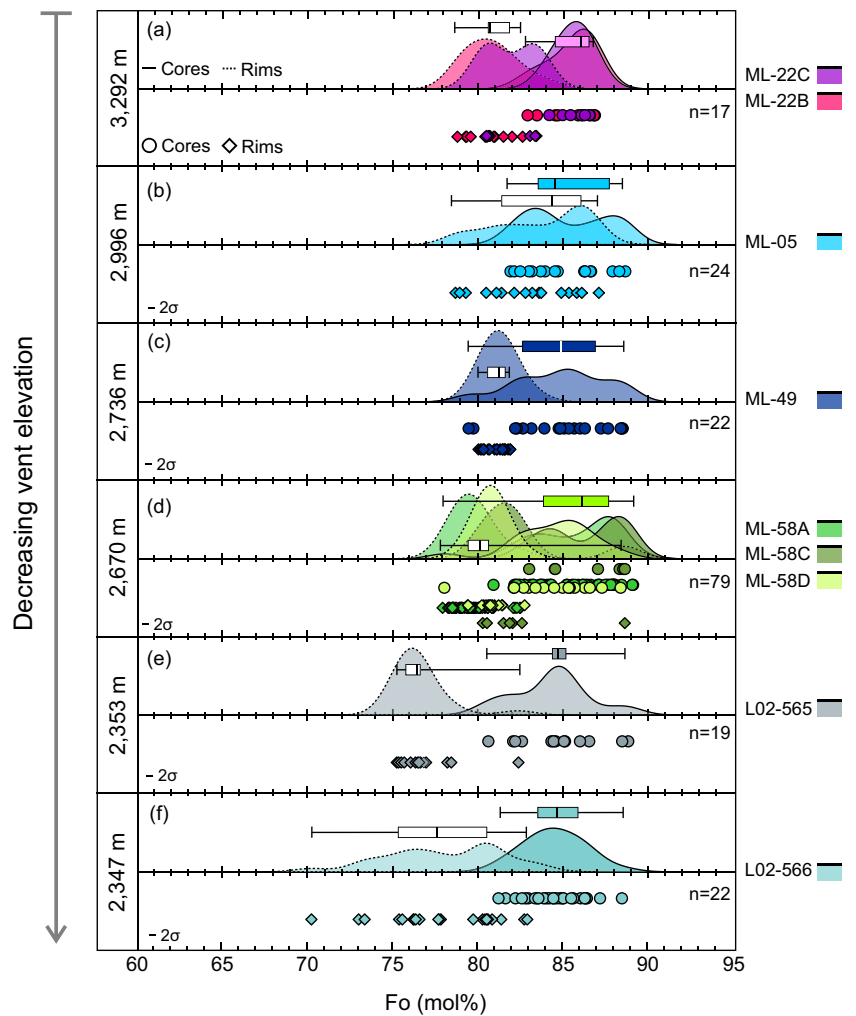
ML-22B and ML-22C olivines (Fig. 3 a) were erupted from an elevation of 3,292 m, having compositions of Fo_{79-87} . Olivine cores are within the range $\text{Fo}_{82.8-86.8}$ with peaks at $\sim \text{Fo}_{86.0}$. Rim compositions range between $\text{Fo}_{78.7}$ and $\text{Fo}_{83.3}$ with a median at $\text{Fo}_{80.7}$.

ML-05 olivines (Fig. 3 b) were erupted from lower elevations at 2,996 m, with compositions of $\text{Fo}_{78.6-88.5}$. Core compositions range between $\text{Fo}_{81.8}$ and $\text{Fo}_{88.5}$ with bimodal peaks at $\sim \text{Fo}_{83}$ and $\sim \text{Fo}_{88}$ (median value: $\text{Fo}_{84.5}$). Olivine rims range between $\text{Fo}_{78.6}$ and $\text{Fo}_{87.0}$, with a median at $\text{Fo}_{84.2}$.

ML-49 olivines (Fig. 3 c) are from vent elevations at 2,736 m, with core compositions between $\text{Fo}_{79.4-88.4}$ and a median of $\text{Fo}_{84.9}$. Olivine rims range between $\text{Fo}_{80.0-81.8}$ with a defined peak at $\text{Fo}_{81.2}$.

ML-58A, ML-58C, and ML-58D olivines (Fig. 3 d) were erupted from the same elevation at 2,670 m. Olivine cores

Fig. 3 Kernel density estimates (KDEs) depicting forsterite content (Fo) distribution of olivine cores and rims from samples that erupted from vents at different elevations along the 1950 AD fissure system. Box plots for olivine core (coloured boxes) and rim (white boxes) compositions with median values (black vertical line). Error bar, 2σ



display the most primitive compositions within the range $Fo_{78.0-89.1}$ (ML-58D: $Fo_{78.0-88.3}$; ML-58C: $Fo_{83.0-88.6}$; ML-58A: $Fo_{80.9-89.1}$), with median values of Fo_{85} (ML-58D) and Fo_{87} (ML-58A and ML-58C) and combined median of $Fo_{86.1}$ (Fig. 3 d). Olivine rims range between $Fo_{77.9}$ and $Fo_{88.6}$ (ML-58D: $Fo_{79.4-82.7}$; ML-58C: $Fo_{80.2-88.6}$; ML-58A: $Fo_{77.9-82.5}$), with peaks at $Fo_{80.7}$ and $Fo_{81.8}$ (ML-58D and ML-58C) and $Fo_{79.6}$ (ML-58A; combined median: $Fo_{80.1}$).

L02-565 and L02-566 olivines (Fig. 3 e, f) were erupted from the lowest elevations at 2353 m (L02-565) and 2347 m (L02-566), showing the largest compositional range between $Fo_{70.2}$ and $Fo_{88.8}$. Olivine cores range between $Fo_{80.6-88.8}$ (L02-565) and $Fo_{81.2-88.4}$ (L02-566), with median values of $Fo_{84.7}$, respectively. Olivine rims are shifted towards more evolved compositions between $Fo_{70.2}$ and $Fo_{82.9}$ with median values of $Fo_{76.5}$ (L02-565) and $Fo_{77.8}$ (L02-566).

Observed overall olivine core compositions ($n=183$) span a wide range between $Fo_{78.0}$ and $Fo_{89.1}$. The vast majority (61%) fall within the range $Fo_{82.5-87}$. Twenty-seven percent are within the narrow range Fo_{87-89} (i.e. compositional range of accumulated high forsterite olivines contained in

historical Mauna Loa picrites; Rhodes 1995), and 12% display more evolved compositions of $Fo_{78-82.5}$ (i.e. compositional range typical for liquidus olivines crystallising from Mauna Loa reservoir lavas; Rhodes 1995).

Minor element (NiO, MnO, CaO, and Ni/Mn) versus forsterite content variation diagrams of the olivine core and rim compositions are shown in figure S7. Olivine cores and rims show a positive correlation between forsterite and NiO (Fig. S7). The cores (Fo_{78-89}) have NiO contents within the range 0.20–0.46 wt% and the rims (Fo_{70-89}) are between 0.14 and 0.38 wt%. MnO displays a negative trend with increasing forsterite content (Fig. S7). Olivine cores and rims range between 0.13–0.26 wt% and 0.16–0.31 wt%, respectively. CaO shows a weak negative correlation with forsterite content (Fig. S7). Core CaO concentration ranges from 0.19 to 0.28 wt% and rims range from 0.21 to 0.49 wt%.

Ni/Mn ratios display a positive trend with increasing forsterite content (Fig. S7). Low-forsterite ($Fo \leq 82$) olivine cores and rims have Ni/Mn ratios between 0.14 and 1.72, whereas high-forsterite ($Fo \geq 87$) olivine cores and rims display ratios ranging from 1.63 to 3.08.

The analysed olivines are also characterised by variable zonation sense and pattern (Figs. 4 and 5). The majority (81%; Fig. 5a) of the olivine crystals are characterised by simple, single-step normal zonation with extensive core plateaux of variable composition (Fo_{78-89}) followed by decreasing forsterite contents towards the rims (Fig. 4a–d). Fourteen percent (Fig. 5a) display complex zoning, with reversely zoned crystal interiors of variable composition (Fo_{78-87}) followed by high-forsterite mantles (Fo_{83-88}) and normally zoned outermost rims with decreasing forsterite contents (Fig. 4a–d). Only five percent (Fig. 5a) of the crystals are characterised by homogenous profiles (flat; Fo_{79-89}).

Based on different core compositional plateaux, six different olivine zoning types (3 normal and 3 complex) can be distinguished (Figs. 4 and 5b). Table 1 lists the

characteristics of each zoning type and their abundance in the studied 1950 sample record.

Olivine-melt equilibria

Groundmass glass and PEC-corrected melt inclusion compositions were used to investigate olivine-melt relationships and to test whether the olivines were in chemical equilibrium with their host melts at the time of eruption. Groundmass glass and PEC-corrected melt inclusion compositions of the 1950 AD eruption products investigated in this study (Fig. 2b) have MgO contents ranging between 5.6 and 10 wt.% with corresponding Mg-numbers ($\text{Mg}\#_{\text{liquid}}$) of 49.2–70.4 (tables S7–S8).

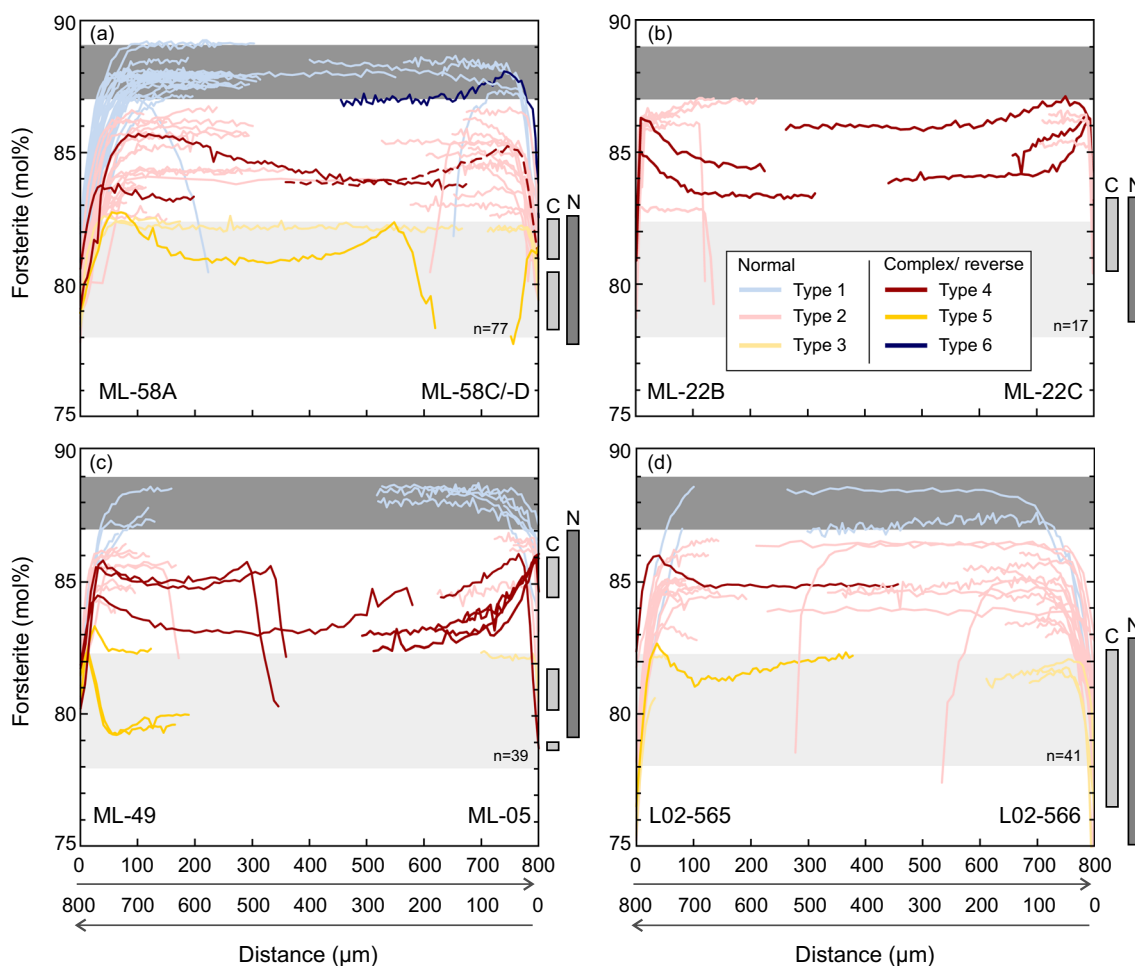


Fig. 4 Olivine zoning patterns. **a–d** Different types of normal (types 1–3) and complex/ reverse (types 4–6) zoning identified in the 1950 AD olivine crystals are distinguished by colour. For more details about zoning types, see main text. Coloured lines: rim-to-core and rim-to-rim forsterite ($100 \times (\text{Mg}/(\text{Mg}+\text{Fe}^{2+}))$) concentration profiles. Dark and bright grey bars next to each plot indicate the range of rim compositions in complex reverse ('C') and normally ('N') zoned olivines. The number of crystals considered ($n=174$) is less than the

total number of crystals ($n=183$). This is deliberate as 5% ($n=9$) of the olivines do not display any systematic zoning pattern and are therefore not considered in this plot. Dark grey shaded area: compositional range of accumulated high forsterite (Fo_{87-89}) olivine cargo identified in historical Mauna Loa picrites (Rhodes 1995). Light grey area: range of typical liquidus olivine compositions (Fo_{78-82}) crystallising from Mauna Loa reservoir lavas (Rhodes 1995).

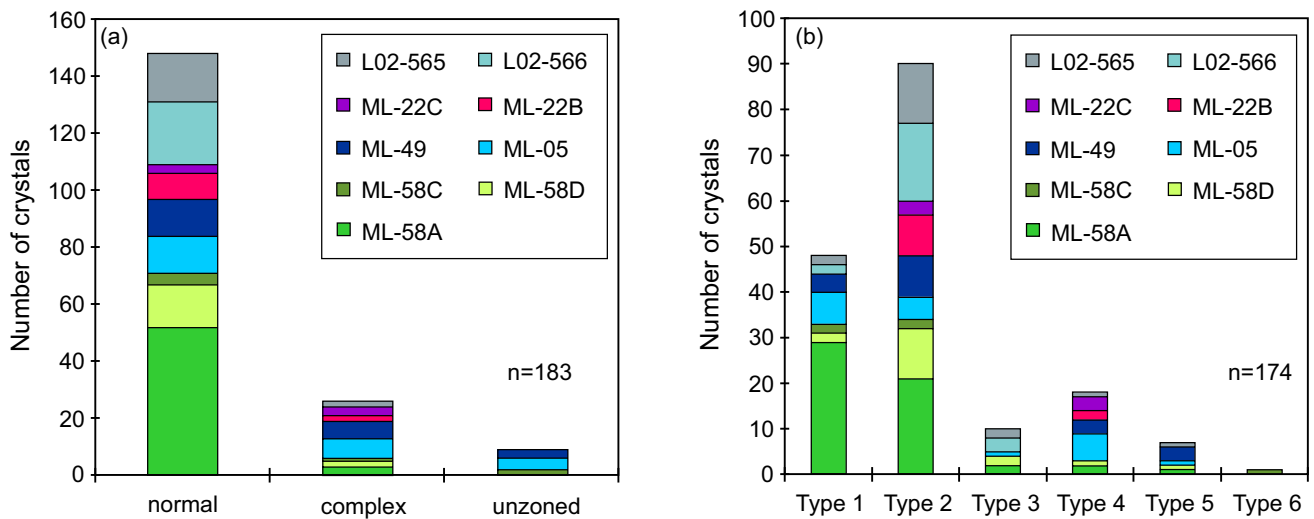


Fig. 5 Frequency distribution of olivine zoning types among the studied 1950 AD samples. **a** Histogram showing the frequency of normally ($n=148$), complexly/reversely ($n=26$), and unzoned ($n=9$) oli-

vine crystals. **b** Histogram detailing the proportion and frequency of the six different zoning types (types 1–3: normal; types 4–6: complex reverse) across the studied sample suite.

Table 1 Summary of olivine zoning types

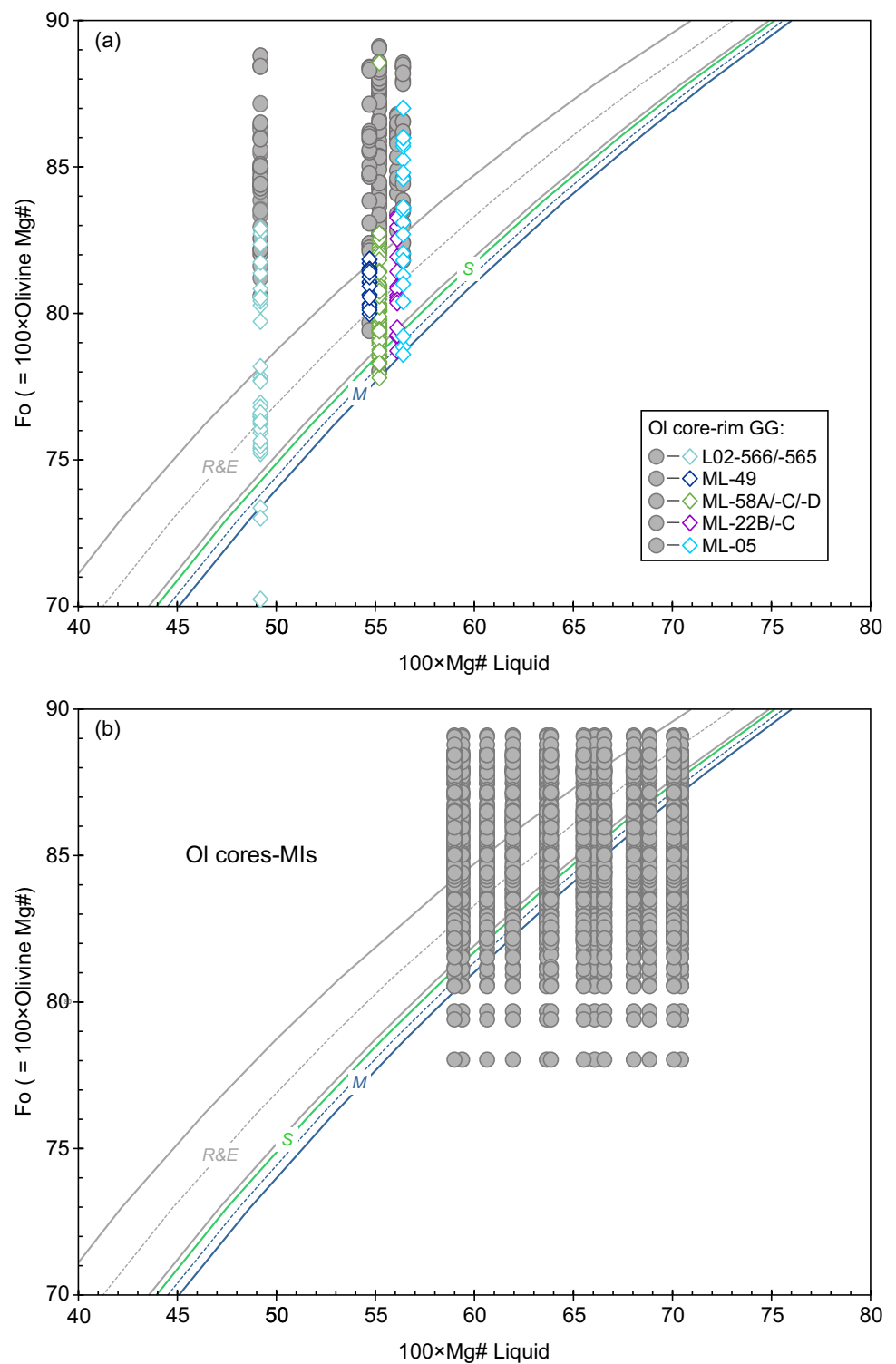
	Type	Abundance	Characteristics
Normal zoning	Type 1	26% ($n=48$)	Normally zoned olivines with extended high forsterite ($>Fo_{87}$) core plateaux and decreasing forsterite contents towards the rims ($Fo_{76.5-87}$). Identified in all samples except ML-22B/ML-22C (Fig. 5b)
	Type 2	49% ($n=90$)	Normally zoned olivines containing core plateau compositions of $Fo_{82.5-87}$ and rim compositions of Fo_{73-85} . Occurs in all studied samples (Fig. 5b)
	Type 3	5% ($n=10$)	Normally zoned olivines with low forsterite ($Fo_{78-82.5}$) core plateaux and decreasing forsterite contents towards the rims (Fo_{70-80}). Occurs in all samples except ML-22B, ML-22C, ML-49 and ML-58C (Fig. 5b)
Complex-reverse zoning	Type 4	10% ($n=18$)	Complexly zoned olivines with reversely zoned crystal interiors ($Fo_{82.5-87}$), mantled by regions with higher forsterite contents ($\sim Fo_{84-87}$) surrounded by normally zoned rims at Fo_{79-86} . Can be found in all samples except ML-58C and L02-566 (Fig. 5b)
	Type 5	4% ($n=7$)	Complex reversely zoned crystals with low forsterite core plateaux at $Fo_{78-82.5}$, mantled by regions with higher forsterite contents ($\sim Fo_{81-83}$) surrounded by normally zoned, less forsteritic rims at $Fo_{76.5-86}$. Minor zoning type, occurs in all samples except ML-58C, ML-22B/C, and L02-566 (Fig. 5b)
	Type 6	1% ($n=1$)	Complex reversely zoned crystal (s) with high forsterite interior (Fo_{87}), followed by a forsterite-rich zone ($\sim Fo_{88}$) and normally zoned, less forsteritic rims ($\sim Fo_{82.5}$). Minor zoning type, could only be identified in ML-58C (Fig. 5b)

Figure 6 illustrates the range of olivine compositions calculated to be in equilibrium with groundmass glasses (Fig. 6a) and PEC-corrected melt inclusions (Fig. 6b) for samples that erupted from different vent elevations (i.e. 3292–2347m). Predicted olivine-melt equilibrium compositions are provided in tables S7 and S8. Equilibrium compositions were calculated using the models of Roeder and Emslie (1970; $K_D = 0.3 \pm 0.03$ [1SEE; standard error of estimate]), Matzen et al. (2011; $K_D = 0.343 \pm 0.008$ [1SEE]), and Shea et al. (2022; $K_D = 0.335 \pm 0.001$

[1SEE]) assuming $Fe^{3+}/Fe^T = 0.15$ (Moussallam et al. 2016; Helz et al. 2017; Wieser et al. 2021; Couperthwaite et al. 2022) to provide the most appropriate envelope for olivine-melt equilibrium calculations.

The majority (87%) of olivine rim compositions (Fo_{73-83}) appear to be in equilibrium with their respective carrier liquids ($Mg\#_{liquid} 49.2-56.4$; $MgO 5.6-6.8$ wt%), with the exception of some more evolved olivine rims (L02-566; Fig. 6a), which appear to have crystallised from melts more evolved than the matrix glass. Most olivine cores (86%) are

Fig. 6 Olivine-melt equilibrium relations. **a** Groundmass glass (GG) Mg numbers ($Mg\# = 100 \times Mg / (Mg + Fe^{2+})$) plotted against olivine core (filled circles) and rim (filled diamonds) forsterite contents. **b** PEC-corrected melt inclusion Mg-numbers plotted against combined olivine core compositions from all samples studied. Grey ('R&E'), blue ('M'), and green ('S') solid curves mark the equilibrium fields for Fe-Mg partitioning of Roeder and Emslie (1970; K_D of 0.3 ± 0.03), Matzen et al. (2011; K_D of 0.343 ± 0.008), and Shea et al. (2022; K_D of 0.335 ± 0.01). Mg numbers were calculated assuming $Fe^{3+}/Fe^T = 0.15$ (Mousallam et al. 2016; Helz et al. 2017; Wieser et al. 2021; Couperthwaite et al. 2022).



more primitive than the carrier liquid compositions (Fig. 6a). They appear, however, to be in equilibrium with a range of primitive melt inclusion compositions ($Mg\#_{liquid}$ 59–70.4; MgO 7.0–10.0 wt%; Fig. 6b).

The combined olivine-melt relationship data allows us to identify phenocrystic (in chemical equilibrium with the

carrier liquid) and antecrystic (not in chemical equilibrium with the carrier liquid but originated in the same magmatic system; e.g. Streck 2008; Davidson et al. 2007) olivine populations. Most 1950 AD olivine rims (87%) represent phenocrystic material, whereas the olivine cores (86%) represent antecrystic material, too primitive to be in equilibrium

with the carrier liquid. This feature is fairly common for Hawaiian olivine cores (e.g. Lynn et al. 2017; Thornber et al. 2003; Thornber 2001; Garcia et al. 2000; Garcia 1996; Garcia et al. 1995; Rhodes 1995) suggesting that they were possibly assembled from different parts of the plumbing system.

Geothermometry

Mineral-melt and melt-only thermometry was applied to constrain the thermochemical conditions of magma storage. Groundmass glass and PEC-corrected melt inclusion temperatures were calculated using the glass-composition-based thermometers of Montierth et al. (Montierth et al. 1995; $SEE = \pm 10^\circ$) and Shea et al. (Shea et al. 2022; $SEE = \pm 13^\circ\text{C}$). Olivine-melt temperatures were calculated using Eqs. 19 and 20 from Putirka (Putirka 2008; $SEE = \pm 44^\circ$) based on the Beattie (1993) model, using the Herzberg and O'Hara (2002) pressure correction. Olivine-melt equilibrium pairs were selected using the updated K_D values of Matzen et al. (2011) and Shea et al. (2022) assuming anhydrous (<1 wt% H_2O ; Hauri 2002) conditions and $\text{Fe}^{3+}/\text{Fe}^T = 0.15$. Orthopyroxene-melt temperatures were calculated using Eqs. 28a ($SEE = \pm 28^\circ\text{C}$) and 28b ($SEE = \pm 48^\circ\text{C}$) from Putirka (2008). Orthopyroxene-melt pairs were filtered carefully following the equilibrium test (i.e., $K_D^{\text{opx-liq}} = 0.4805 - 0.3773 \times x_{\text{Si}}^{\text{liq}}$) outlined in Putirka (2008). Equilibrium was considered if $\Delta K_D^{\text{opx-liq}}$ values were within ± 0.06 of equilibrium values assuming anhydrous (<1 wt% H_2O) conditions and $\text{Fe}^{3+}/\text{Fe}^T = 0.15$. To retrieve the full thermal history, we aimed at matching macrocryst cores with PEC-corrected melt inclusion ($\text{Mg}\#_{\text{liq}} 59\text{--}70$) and rims with groundmass glass ($\text{Mg}\#_{\text{liq}} 48\text{--}58$) compositions. Some rim compositions in reversely zoned olivine and orthopyroxenes are more primitive than the groundmass glass compositions; hence, those were matched with melt inclusion compositions. Kernel density estimates (KDEs) showing melt-only and mineral-melt temperature distributions for the Mauna Loa 1950 AD samples are summarised in figure S8.

Olivine and orthopyroxene cores ($\text{Fo}_{78\text{--}88}$; $\text{Mg}\#_{75\text{--}84}$) record temperatures within the range $1174\text{--}1269^\circ\text{C}$ with mean values of $1226 \pm 25^\circ\text{C}$ and $1213 \pm 15^\circ\text{C}$. Rims ($\text{Fo}_{73\text{--}87}$; $\text{Mg}\#_{76\text{--}85}$) record slightly lower temperatures of $1151\text{--}1265^\circ\text{C}$ with means of $1185 \pm 14^\circ\text{C}$ and $1205 \pm 18^\circ\text{C}$ (Fig. S8).

Glass temperatures are widely consistent with mineral-melt temperatures recording $1135\text{--}1172^\circ\text{C}$ with mean values of $1158 \pm 8^\circ\text{C}$ (Montierth et al. 1995) and $1151 \pm 7^\circ\text{C}$ (Shea et al. 2022) for groundmass glasses. Primitive PEC-corrected melt inclusions ($\text{Mg}\#_{\text{liq}} 68\text{--}70.4$) register $1213\text{--}1243^\circ\text{C}$ with mean values of $1237 \pm 6^\circ\text{C}$ (Montierth et al. 1995) and $1225 \pm 6^\circ\text{C}$ (Shea et al. 2022). Intermediate MIs ($\text{Mg}\#_{\text{liq}} 59\text{--}67$) record temperatures of $1166\text{--}1215^\circ\text{C}$ with means of $1199 \pm 13^\circ\text{C}$ (Montierth et al. 1995) and $1190 \pm 12^\circ\text{C}$ (Shea et al. 2022).

We note that glass temperatures reflect the same variations as whole-rock and glass compositions with decreasing vent elevation. Glass temperatures increase with decreasing vent elevation reaching a maximum of $1172 \pm 3^\circ\text{C}$ (Montierth et al. 1995) ($\text{Mg}\#_{\text{liquid}} 58$; 7.3 wt% MgO) at an elevation of ~ 2963 m before decreasing again (table S7).

Diffusion chronometry

One hundred three time estimates from modelling the diffusive relaxation of Fe-Mg zoning profiles in 93 olivine crystals have been obtained using *Autodiff*, an objective, rapid-modelling approach that exploits the self-similarity of one-dimensional diffusion profiles with similar boundary conditions to allow timescales to be determined quickly (Kahl et al. 2022; Couperthwaite et al. 2021, 2020; Pankhurst et al. 2018; Allan et al. 2017; Hartley et al. 2016). Of the 183 olivine crystals analysed, only 93 were suitable for diffusion modelling. Nine crystals were unzoned and the remaining 81 olivines were rejected due to either (1) analytical difficulties or (2) the compositional gradient in the profiles was noticeably affected by crystal growth and/or apparent changes in boundary conditions (Couperthwaite et al. 2020). We applied step (square wave) or externally buffered boundary conditions depending on the shape of the concentration profile and its position within the crystal. In this study, we focused on Fe-Mg zoning in olivine, using the updated (corrected) version of the Fe-Mg diffusion coefficients obtained by Dohmen et al. (2007) and Dohmen and Chakraborty (2007) as quoted in Chakraborty (2010), accounting for composition dependence, anisotropy, oxygen fugacity, and potentially variable diffusion mechanism. Anisotropy-corrected diffusivities were calculated by *Autodiff* for each traverse based on the angles between the analytical traverse and the olivine's *a*-, *b*-, and *c*-axes. For this purpose, the orientation and the angular relation of the crystallographic *a*-, *b*-, and *c*-axes in the analysed olivine crystals were determined using EBSD (see Analytical Methods, Supplementary Material and table S9). A detailed explanation of the *Autodiff* diffusion modelling approach is provided in Couperthwaite et al. (2020, 2021) and Kahl et al. (2022). Examples of best-fit models are shown in Fig. 7 (modelling results are provided in table S10). The number of independent estimates ($n=103$) is larger than the number of crystals modelled ($n=93$) because some crystals record multistage events, which were modelled stepwise.

Olivines were modelled using temperatures of $1154\text{--}1188^\circ\text{C}$ for the rims and $1234 \pm 6^\circ\text{C}$ for the interiors of complex reversely zoned crystals. The selected temperatures are consistent with constraints using olivine-liquid (Eqs. 19 and 20; Putirka 2008) and liquid-only thermometry (Montierth et al. 1995; Shea et al. 2022) in groundmass glasses and olivine-hosted melt inclusions. For all models, oxygen

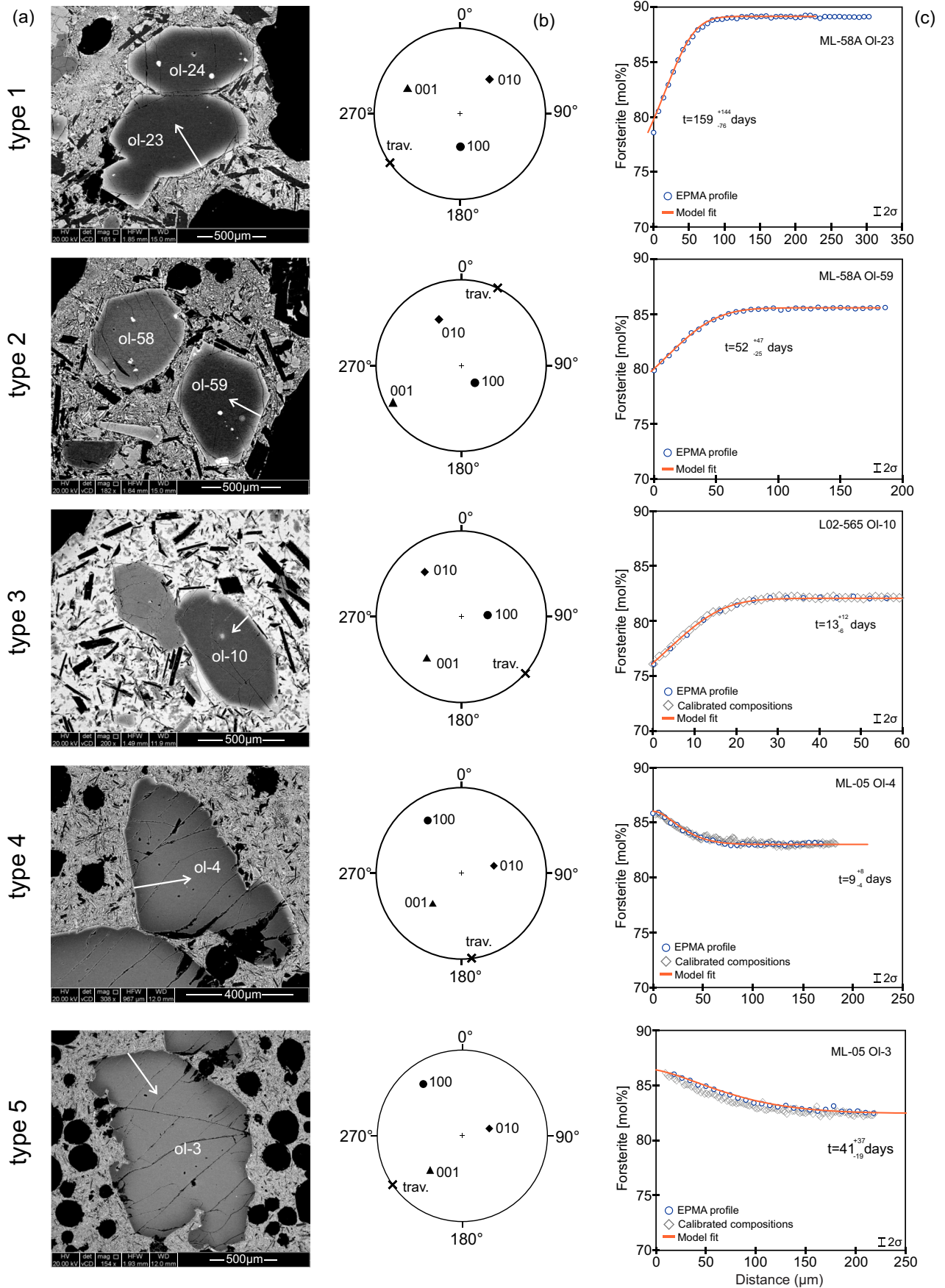


Fig. 7 Data and best-fit olivine Fe-Mg diffusion models for the different olivine populations (types 1–5) identified in the 1950 AD samples. **a** Backscattered electron (BSE) images of analysed olivine macrocrysts. White arrows: positions of microanalytical traverses. **b** Stereographic lower-hemisphere plots depicting the angular relations between the main crystallographic axes in olivine and the directions of analytical traverses ('x' marked 'trav.'). **c** Measured electron microprobe (EPMA; filled circles) and BSE calibrated (grey diamonds) forsterite rim-to-core profiles. Orange curves: best-fit diffusion models and calculated uncertainties.

fugacity conditions were set at the QFM buffer (e.g. Gerlach 1993; Couperthwaite et al. 2022). Due to a general paucity of robust magma storage depth constraints for Mauna Loa in comparison to neighbouring Kīlauea volcano, we decided to set pressures for the olivine diffusion models to a maximum of 0.38 GPa. This is consistent with the maximum depth (~ 15 km) of seismicity that was detected preceding the 1975, 1984, and 2000 AD eruptions of Mauna Loa (see 'Discussion' below). Although pressure has a negligible effect on diffusion model uncertainties, we note that the compositional and textural heterogeneity inherent to the 1950 AD crystal cargo suggests complex and possibly multilevel magmatic storage histories (see 'Discussion' below). To account for multilevel magma ponding and crystal entrainment, we have calculated the effect different pressures have on the overall diffusion modelling timescales. For instance, modelling type 2 and 4 ($\text{Fo}_{82.5-87}$) olivines at pressures (~ 0.27 GPa) corresponding to intermediate level storage and magma mixing (~ 10 km; depth of the décollement between the volcano and the oceanic crust, e.g. Wilding et al. 2023; see 'Discussion' below) will reduce the diffusion modelling timescales by ~ 5% on average (i.e. 65 days will reduce to 62 days). More evolved types 3 and 5 ($\text{Fo}_{78-82.5}$) are similar in composition to typical reservoir lava olivines (Fo_{77-82} ; Rhodes 1995). Hence, modelling these more evolved olivine types at pressures (<0.1 GPa) corresponding to the depths of the shallow summit magma reservoir (~ 3–5 km; Rhodes 1988; Garcia et al. 1995; Rhodes 1995) will reduce the diffusion timescales by ~ 9% on average (i.e. 65 days will reduce to 59 days). Primitive type 1 and 6 (Fo_{87-89}) olivines coexisting and intergrown with Mg-rich orthopyroxene (Mg#) indicating deep, near-Moho (~ 0.6 GPa) magma storage will increase the diffusion timescales by ~ 8% on average (i.e. 65 days will increase to 70 days). The observed changes in the diffusion timescales are minimal and within the calculated 1 sigma uncertainty of ± 0.28 log units on each timescale.

Modelling complex crystals—combined diffusion and growth

Initially, all zoning types were considered for modelling with *Autodiff*, with the more complexly zoned types 4, 5, and 6 broken into two segments representing internal reverse

zones and external normal zoning. Simplistic modelling of the reverse zones using rim temperatures typically yields long timescales of hundreds to thousands of days, in contrast with normally zoned rims of much shorter duration. Despite in some cases quite good fits to curves, we believe that simplistic models in this case are potentially misleading. First, reverse zones, especially ones that link up with later normal zoning, do not preserve a defined plateau composition for the high-forsterite end of the model. Therefore, any high forsterite value that is preserved in the profile will be an underestimate relative to the true value that drove diffusion. Second, it is reasonable to infer that the high forsterite values present in these zones may represent residence at higher temperatures than the rim equilibrium. Therefore, any diffusion modelling that uses the rim equilibria to inform temperature may significantly underestimate the related timescale through being unrealistically cold. Combining the two aspects, temperatures may have been required which exceed those related to any forsterite value preserved in the post-diffusion profile. A further consideration is that type 4 and type 5 profiles show reverse and normal components that interact diffusively. To run them independently is to impose an artificial division into the profile which is not borne out by subsequent evolution. To reconcile this, we have expanded upon the variable boundary-condition modelling used by Couperthwaite et al. (2021), to undertake modelling with variable boundary conditions which allow for heating and cooling as well as crystal growth. Details of the combined diffusion and growth (CDG) modelling applied to model complex olivine zoning are provided in the Supplementary Material and table S10.

Overall olivine Fe-Mg diffusion timescales calculated in this study range between 1 and 572 days (~ 1.6 years) with an average uncertainty on each timescale of ± 0.28 log units (1σ). The median timescale is 43 days with 71% ($n=73$) of the timescales being shorter than 3 months (~ 92 days).

Discussion

Conditions and depth of magma storage

Although magma storage depths beneath Mauna Loa are less well-constrained than for neighbouring Kīlauea, the existence of discrete storage zones characterised as regions of high seismic velocities (6.5–7.5 km/s) has been identified at a depth range of ~ 0–10 km beneath the summit and ~ 0–6 km beneath Mauna Loa's lower SWRZ (Couperthwaite et al. 2022; Poland et al. 2014; Lin et al. 2014; Park et al. 2007; Okubo et al. 1997). This depth range roughly coincides with the depths of shallow- (0–5 km) and intermediate-level (5–15 km) seismicity preceding the 1975 (NE and SW rift zone) 1984 and 2022 (NERZ) AD eruptions of Mauna Loa (Lockwood et al. 1987; Decker et al. 1995; Couperthwaite et al. 2020). A shallow

magma reservoir at a depth of 3–4 km beneath the summit caldera of Mauna Loa has been identified by Decker et al. (1983) coinciding with the detection of high seismic velocity bodies in this region. Recent efforts combining high-resolution earthquake relocation with deep learning algorithms enabled mapping of potential magma pathways connecting a deep (36 to 43 km) and extensive (15 km long) mantle sill complex (Pāhala sill complex) with the plumbing networks of Kīlauea and Mauna Loa following the 2018 Kīlauea caldera collapse (Wilding et al. 2023). The seismic structure (Pāhala-Mauna Loa seismicity band) connecting the Pāhala sill complex with the edifice of Mauna Loa terminates beneath the décollement, a zone with a clustering of long-period earthquakes at a depth of 10 km (Wilding et al. 2023).

Despite the wealth of geophysical data, robust geobarometric constraints of pre-eruptive magma storage depths for Mauna Loa are scarce. Thermodynamic modelling of compositionally diverse Mauna Loa xenoliths from the SWRZ (Gaffney 2002) suggests polybaric crystallisation of primitive Mauna Loa magmas within at least two distinct regions at ~ 7 km (0.2 GPa), just above the décollement (~ 10 km; e.g. Wilding et al. 2023; Matoza et al. 2020), and at ~ 21 km (0.6 GPa) just below the Moho (~ 18 km; Hill and Zucca 1987). Multilevel crystallisation conditions are further supported by the variable location of orthopyroxene in the crystallisation sequence (as second or fourth phase to crystallise) of the xenoliths phase assemblages (Gaffney 2002). This agrees, for instance, with the occurrence of primitive, Mg-rich ol-opx (harzburgite) glomerocrysts in the 1950 AD eruption products. Olivines in the 1950 AD samples occur as large, polyhedral macrocrysts but also as mono- (dunite) or various types of polymineralic glomerocrysts (see figure S2) including lherzolites (ol-opx-cpx), harzburgites (ol-opx), troctolites (ol-plag), pyroxenites (opx-cpx), gabbroic (pl-cpx), and gabbro-norite (pl-opx-cpx). Glomerocrysts often display irregular, rounded shapes, and interstitial space between faces of touching crystals is often filled with glass (melt) indicating a crystal-liquid mush origin (e.g. Gaffney 2002; Nakagawa et al. 2002; Jerram et al. 2003; Couperthwaite et al. 2022).

Although robust geobarometric constraints of pre-eruptive magma storage depths are scarce for Mauna Loa, thermodynamic modelling and phase-relation experiments on Hawaiian olivine-tholeiites indicate that orthopyroxene joins olivine as a liquidus phase at pressures higher than 0.6 GPa (Wanless et al. 2006; Maaløe 2004; Gaffney 2002; Eggins 1992; Green and Ringwood 1967). We therefore argue that coexisting Mg-rich olivine and orthopyroxene and the occurrence of primitive ol-opx (harzburgite) glomerocrysts (Fig. S2) in the 1950 AD eruption products may represent a primary and possibly deeper, near- or sub-Moho phase assemblage (e.g. Thornber and Trusdell 2008). Due to the lack of well-calibrated mineral-melt barometers for thin crusted systems such as Hawai'i, precise determination of pre-eruptive magma storage depths

for Mauna Loa remains challenging (Wieser et al. 2023). In the future, more precise quantitative geobarometric studies are required to reconcile petrologically constrained conditions of magma storage with emerging geophysical models of deep magma storage and transport beneath Mauna Loa.

Intricate magma plumbing dynamics indicated by heterogeneous crystal cargo

The compositional heterogeneity and the diverse zoning preserved within the 1950 AD olivine cargo indicate complex petrogenetic histories of crystal evolution, inheritance, and recycling within diverse parts of Mauna Loa's magma storage and transport system. The occurrence of different zoning types (normal vs. complex reverse) with variable core compositional plateaux (Fo_{78-89}) and the coexistence of primitive and evolved crystal populations reflect crystal evolution and storage within distinct magmatic environments. Antecrystic primitive (Fo_{87-89}) cores contained in normally (type 1; 26%) and rare complex reversely (type 6; 1%) zoned olivines return the highest temperatures (1261 ± 10 °C), consistent with primitive melt inclusion (1237 ± 6 °C) and Mg-rich ($\text{Mg}_{\#84}$) orthopyroxene core (1236 ± 4 °C) temperatures, suggesting primitive macrocryst core formation within hotter and likely deeper parts of Mauna Loa's magmatic system. Common type 2 (normal zoning; 49%) and type 4 (complex reverse zoning; 10%) olivines have intermediate core ($\text{Fo}_{82.5-87}$) compositions returning somewhat lower temperatures (1224 ± 12 °C) consistent with intermediate ($\text{Mg}_{\#_{\text{liq}}} 59-67$) melt inclusion (1199 ± 13 °C) and intermediate orthopyroxene core ($\text{Mg}_{\#81-83}$) temperatures (1217 ± 7 °C), probably indicating deep or intermediate (~ 10 km; corresponding to the depth of the décollement; e.g. Wilding et al. 2023; Matoza et al. 2020) level crystal evolution. In contrast, more evolved and mostly phenocrystic olivine cores ($\text{Fo}_{78-82.5}$) occurring in rare type 3 (normal zoning; 5%) and type 5 (complex reverse zoning; 4%) crystals, plus evolved, but corroded orthopyroxene ($\text{Mg}_{\#75-80}$) cores record the lowest temperatures (1191 ± 5 °C and 1196 ± 9 °C), consistent with groundmass glass (1158 ± 8 °C) temperatures, reflecting evolved macrocryst core formation within cooler and possibly shallower (~ 3–5 km; e.g. Garcia et al. 1995; Rhodes 1995; Rhodes 1988; Decker et al. 1983) parts of Mauna Loa's plumbing system.

Reverse and complex zoning patterns have been interpreted as indicators for open system processes including magma recharge and magma mixing (Streck 2008 and references therein). More recently, the occurrence of reverse zoning in olivine crystals from Kīlauea has been interpreted as a proxy for multiple recharge of primitive melts (Mourey et al. 2023).

High (Fo_{84-88}) and intermediate (Fo_{81-83}) forsterite shoulder zones featuring in complex reversely zoned type

4, 5, and 6 olivines record temperatures of 1270–1286 °C (Fo_{85-87}) and 1203–1208 °C (Fo_{82-83}) reflecting magma recharge, mixing, and crystal entrainment processes within different levels of Mauna Loa's plumbing system. Observed compositional and textural diversity including evidence for basaltic cannibalism (e.g. Cashman and Blundy 2013) in the form of complex, reversely zoned macrocrysts; resorbed antecrystic cores; and compositionally diverse crystal populations is not limited to olivine but can also be tracked within other macrocryst phases including orthopyroxene and clinopyroxene (see figures S3 and S4).

Multilevel crystallisation conditions, combined macrocryst variability and texturally diverse glomerocryst and macrocryst populations, point to the existence of a network of ephemeral, but possibly interconnected magma pockets, ranging from near-Moho depths to the upper/mid-crust underneath Mauna Loa's SWRZ (e.g. Wilding et al. 2023; Gaffney 2002; Klügel and Klein 2006; Stroncik et al. 2009). Dense, Mg- and olivine-rich magmas reside within the deepest, near- to sub-Moho parts of Mauna Loa's SWRZ bypassing the shallow summit reservoir (Garcia et al. 1995; Gaffney 2002). These magmas have intruded along density contrast boundaries (e.g. Moho) and are preferentially erupted from the distal regions (i.e. flanks) of the SWRZ during episodes of high magma supply carrying a primitive olivine cargo with a wide range of compositions (Fo_{82-91} ; most frequent Fo_{89-90}) and predominately normal zoning (Garcia et al. 1995). During episodes of low magma influx, these deep storage areas remain isolated and undisturbed. During periods of increased magma supply, however, dense, MgO- and olivine-rich magma that normally resides in the deep roots of Mauna Loa's plumbing system migrates to shallower depths (~ 3–5 km; Garcia et al. 1995; Rhodes 1995; Rhodes 1988; Decker et al. 1983), where it either fills isolated magma storage areas (followed by cooling and crystallisation) or flushes more differentiated, summit-reservoir-type magmas (6.7–8.0 wt% MgO; Rhodes 1995) that reside within magma storage zones (e.g. Garcia et al. 1995; Gaffney 2002).

We propose that the observed thin-section-scale complexity in those 1950 AD SWRZ samples is caused by complex recharge, mixing, and transport processes. Individual storage zones underneath the SWRZ appear to get flushed by repeated injections of MgO-richer (~ 10 wt%; PEC-corrected melt inclusions, this study) magma residing in the deep roots of Mauna Loa's conduit system. This results in genetically diverse phenocryst and glomerocryst populations originating within different parts and depths of the plumbing network.

Antecrystic type 1 and type 6 (Fo_{87-89}) olivine and primitive orthopyroxene ($Mg\#_{84}$) macrocrysts and glomerocrysts (e.g. harzburgites, dunites) represent near Moho magma storage and mixing within a crystal-rich, mushy reservoir underneath Mauna Loa's SWRZ. Timescales associated with the disaggregation and mobilisation of this deep-seated

mush are represented by type 1 olivines and range between 30 days and 1.4 years (521 days). Magmatic upheaval in this deep-seated mush zone commenced and became gradually more frequent in the ~ 8 months before the eruption (Fig. 8), preceding the onset of increased seismic activity at Mauna Loa by roughly 2 months (e.g. Finch and Macdonald 1951). During periods of increased magma supply into this near-Moho storage region, type 1 olivines, Mg-rich orthopyroxene cores, and primitive glomerocrysts (dunite and harzburgite) were scoured and entrained into hotter and more primitive melts (up to 10 wt% MgO). As the intensity of deep magma supply increased, either different levels of this compositionally and potentially thermally stratified crystal-mush reservoir became gradually remobilised (e.g. Burgisser and Bergantz 2011). Another possible explanation is that individual, compositionally, and spatially diverse, magma pockets were reactivated. This is supported by type 2 (normal zoning) and type 4 (complex reverse zoning) olivine diffusion recorders starting 4 to 6 months before the eruption and the overall increase in the frequency of crystal melt disequilibria (increase in gradient in Fig. 8 between mid-November 1949 and late January 1950). This along with the observed compositional and textural diversity of macro- and glomerocryst populations provides strong evidence for the existence of small, isolated magma pockets, where mixing and cooling of distinct magma batches occur (e.g. Gaffney 2002; Stroncik et al. 2009). More evolved type 3 (normal zoning) and type 5 (complex reverse zoning) olivines and the occurrence of gabbroic glomerocrysts are likely to reflect shallow-level (~ 3–5 km) magma storage and mixing. Intrusive activity into the shallow levels of Mauna Loa's SWRZ plumbing system commenced ~ 2.5 months prior to eruption onset, between mid-March and mid-April 1950, recorded by type 3 and type 5 olivines (Fig. 8) and was accompanied by a strong earthquake on March 25 that was felt across the island (e.g. Finch and Macdonald 1953; <https://www.usgs.gov/volcanoes/mauna-loa/1950-mauna-loas-fastest-high-volume-eruption>). In the weeks and days before the eruption onset, diffusion data show increased frequency of disequilibrium onset (increased gradient in Fig. 8, between mid- and late May 1950), which is synchronous with records of earthquake swarms detected between late May (magnitude 6.4 earthquake on May 29 beneath the Mauna Loa's west flank) and early June (June 1 to 2; not shown in Fig. 8) immediately preceding and accompanying the eruption onset on June 1, 1950 (Finch and Macdonald 1953; <https://www.usgs.gov/volcanoes/mauna-loa/1950-mauna-loas-fastest-high-volume-eruption>). Concurrently, rapid accumulation of eastward tilting of the ground was detected at the Hawaiian Volcano Observatory (HVO) Whitney station between May 29 and June 14, 1950 (Finch and Macdonald 1953). We note that the 1950 AD eruption occurred before the era of high quality, modern, digitally recorded seismic instrumentation,

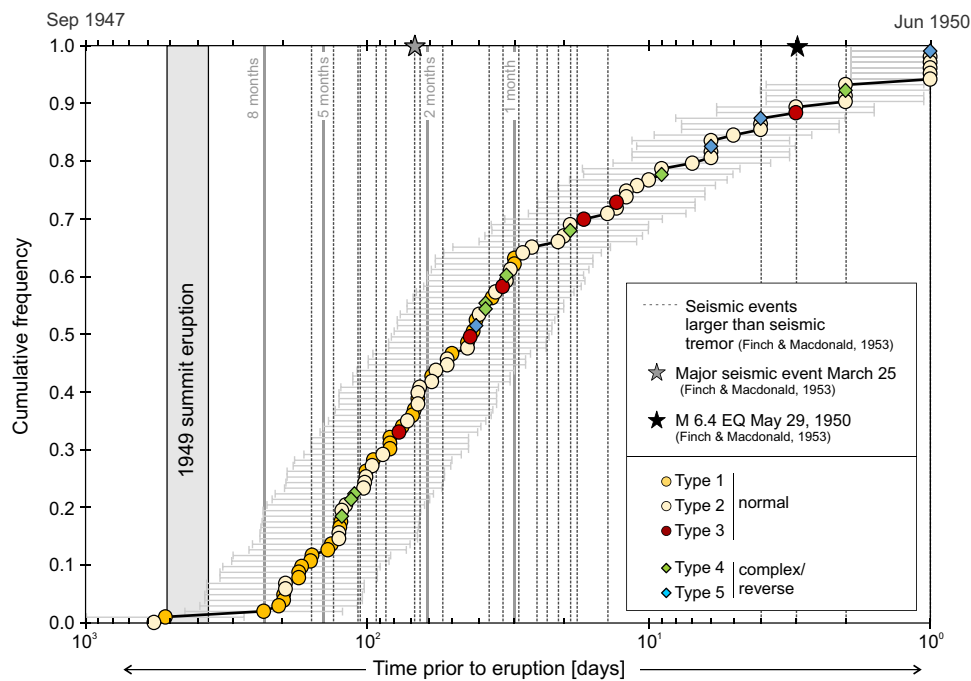


Fig. 8 Rank order plot displaying olivine Fe-Mg diffusion chronometry timescales compared to presumed seismic eruption precursors. Symbols depict cumulative frequency of olivine diffusion timescale records from the 1950 AD samples. Error bars represent an average uncertainty on each timescale of ± 0.28 log units. Timescale data ($n=103$) are colour and symbol coded based on zoning types. Grey shaded box indicates duration of the 1949 summit eruption at Mauna

Loa. Grey stippled lines depict seismic events larger than tremor detected at the Hawaiian Volcano Observatory (HVO) between late December 1949 and late May 1950. Grey star: major earthquake on March 25, 1950. Black star: magnitude 6.4 earthquake on May 29, 1950. Seismic data are from Finch and Macdonald (1953). Seismic data used in this study are provided in table S11. X-axis shows time (in logarithmic scale) in days prior to eruption.

which began with the 1975 eruption (Okubo and Wolfe 2008). As such, the available data of seismic unrest preceding the 1950 AD eruption (Finch and Macdonald 1951, 1953) are not necessarily comparable with the quality and sensitivity of modern seismic records (e.g. Wilding et al. 2023). In particular, the inability and the lack of resolution to detect small ($<M2$) and deep earthquakes impede precise determination of the onset of seismic unrest related to the 1950 AD Mauna Loa eruption.

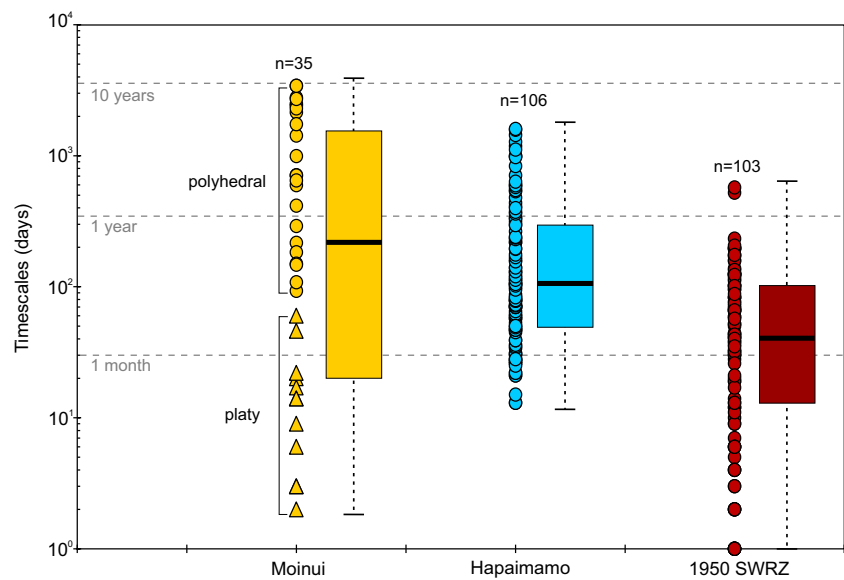
Comparison with mush mobilisation timescales from other Mauna Loa eruptions

The studies of Couperthwaite et al. (2020: 2.1 ka Moinui eruption; and 2022: 240 y B.P. Hapaimamo eruption) provide the first diffusion chronometry records of pre-eruptive magma plumbing dynamics for pre-historic Mauna Loa eruptions. In lava samples from the 2.1 ka Moinui eruption, which erupted from the South Caldera of Mauna Loa, Couperthwaite et al. (2020) identified two morphologically and compositionally distinct olivine populations: a primitive, polyhedral olivine population with core compositions of Fo_{88-90} (similar to type 1 olivines identified in this study) and a more evolved, platy olivine population with core compositions of Fo_{82-83} . Polyhedral olivines display rim

compositions within a narrow range of Fo_{83-84} overlapping with core compositions of platy olivines. Rim compositions of platy olivines are more evolved and also more variable within the range Fo_{65-78} . Both olivine populations display mostly normal zoning (Fe-rich rim, Mg-rich core). The high whole-rock MgO content (14–22 wt%) and its high olivine abundance define the 2.1 ka Moinui lavas as picrites (Couperthwaite et al. 2020 and refs. therein). The olivine cargo differs not only in composition and crystal morphology (polyhedral vs. platy) but also in the calculated Fe-Mg diffusion timescales. Polyhedral, primitive olivines record diffusion timescales on the order of 3 months (93 days) to ~9.3 years (3413 days), whereas evolved, platy olivines record much shorter timescales on the order of 2 days to ~9 weeks (60 days). The overall median timescale is 216 days (~7 months; Fig. 9).

Lava flow and tephra olivines that erupted during the 240 y B.P. Hapaimamo eruption on the lower slopes (~1880 m a.s.l.) of the SWRZ have core compositions between Fo_{81-89} (94% Fo_{84-88} ; lava flow; similar to types 1 and 2 identified in this study) and Fo_{84-89} (80% Fo_{87-89} ; tephra; similar to type 1 identified in this study). Both lava and tephra olivines display normal zoning with rim compositions of Fo_{71-82} (lava flow olivines) and Fo_{81-86} (tephra olivines; Couperthwaite et al. 2022). Although whole-rock

Fig. 9 Compilation of olivine diffusion records for Mauna Loa eruptions modified from Couperthwaite et al. (2022). Filled symbols and adjacent box-whisker plots represent the full range of observed timescales in each study, with black, horizontal bars in box-whisker plots indicating median timescale values. From left to right: 2.1 ka Moinui eruption, Couperthwaite et al. (2020); 240 y B.P. Hapaimamo eruption, Couperthwaite et al. (2022); 1950 AD eruption, this study. Timescales on vertical axis are in log scale.



MgO contents of the Hapaimamo samples are considerably lower (8.1–9.9 wt%) than for the Moinui samples (14–22 wt%), their matrix glass compositions have identical MgO contents (6.6–7.0 wt% for Hapaimamo; 6.6–6.8 wt% for Moinui). Modelled Hapaimamo olivine timescales are slightly shorter ranging between 13 days and ~ 4.4 years (1600 days) with a median value of 104 days (~ 3 months; Fig. 9). Interestingly, the shortest timescales recorded in Hapaimamo olivines are on the order of 13 days (9 days when accounting for uncertainties; Couperthwaite et al. 2022), suggesting that mush disaggregation activity ceased in the week before the eruption.

In comparison, samples from the recent 1950 AD eruption contain compositionally and texturally heterogeneous macrocryst and glomerocryst cargoes recording complex petrogenetic histories of crystal evolution and inheritance from different parts of Mauna Loa's plumbing network, including evidence for mixing between more evolved, shallow stored magma with batches of more primitive and usually deep stored magma. Similarly, complex crystal cargoes with up to six different olivine populations reflecting diverse pre-eruptive magmatic histories have also been reported for the 1868 picrite eruption of Mauna Loa (Schleicher 2017; Rhodes 1995). The 1950 AD olivine diffusion record indicates overall shorter mush disaggregation and mixing timescales on the order of 1 day to ~ 8 months, with a median value of 43 days (~ 6 weeks; Fig. 9).

Comparison of olivine diffusion age records from historical and recent SWRZ eruptions of Mauna Loa indicates that pre-eruptive timescales of mush disaggregation and mobilisation may decrease approaching present time. Given that this comparison is only for three eruptions, it is not clear yet whether these differences represent

inherent variabilities of the respective crystal cargoes or if they reflect general differences/changes in the eruption triggering dynamics. More diffusion chronometry studies on recent Mauna Loa eruptions are required to fully understand and confirm these differences in crystal diffusion age records and their potential link to eruption priming dynamics.

Conclusions

We have presented a combined geochemical, geothermometric, and diffusion chronometry study of conditions of pre-eruptive magma storage and timescales of deep mush disaggregation and mobilisation in the run-up towards the 1950 AD SWRZ eruption of Mauna Loa, the most voluminous SWRZ eruption since written records have been kept. Our main findings are as follows:

1. Detailed petrologic examination unveils compositionally and texturally heterogeneous macrocryst and glomerocryst cargoes suggesting intricate petrogenetic histories of crystal evolution, inheritance, and recycling within diverse parts of Mauna Loa's magmatic system, including evidence for mixing between primitive, deep stored magma, and pockets of more evolved, shallow stored magma.
2. Multilevel crystallisation conditions, combined macrocryst variability, and texturally diverse glomerocryst and macrocryst populations indicate the existence of a network of spatially diverse, ephemeral, but possibly interconnected magma pockets, ranging from near-Moho depths to the upper/mid-crust underneath Mauna Loa's SW rift. The abundance of primitive olivines and the

relative paucity of typical reservoir-type olivines (i.e. Fo₇₇₋₈₂; Rhodes 1995) in samples considered in this study support the idea that the 1950 AD magma storage and transport occurred mainly within the SWRZ plumbing rather than within the central reservoir system.

3. Identification of six different olivine types linked with Fe-Mg diffusion chronometry enables the chronology of events leading to the 1950 AD eruption to be reconstructed. Starting roughly one and a half years prior to eruption and becoming gradually more frequent in the 8 months before, the disaggregation of a deep-seated (near-Moho) primitive crystal mush consisting of type 1 (Fo₈₇₋₈₉) olivine cores and Mg-rich (Mg#₈₄) orthopyroxenes commenced via the intrusion of hotter and more primitive melts from depth. Increased magma supply into this near-Moho storage zone resulted in the remobilisation of the deep-seated mush and the gradual entrainment and onward transport of the primitive crystal cargo. Commencing between 6 and 4 months prior to eruption onset, the MgO- and olivine-rich magma that usually resides at depth migrated to intermediate levels (~ 10 km), flushing more evolved magma pockets as evidenced by an overall increase in the formation of crystal disequilibria and the onset of type 2 and type 4 (Fo_{82.5-87}) olivine diffusion recorders. Beginning ~ 2.5 months before the eruption and continuing until eruption onset, the shallow level storage zone was intruded, recorded by type 3 and type 5 olivines. The rise of deep magma to shallow levels was accompanied by a strong earthquake on March 25, 1950, 2 months before the eruption. Magma supply from depth and mush disaggregation remained high during the following weeks running in parallel with increased seismic activity culminating in a magnitude 6.4 earthquake, on March 29, and immediate-term seismic swarms in late May and early June preceding and accompanying the eruption onset on June 1, 1950.

The combined petrological and diffusion chronometry record presented in this study indicates rapid transport and remobilisation of large volumes of magma ($376 \times 10^6 \text{ m}^3$) from near-Moho storage to the surface within less than 8 months. Residence in the shallow system (~ 3–5 km) is on the order of days, to a maximum of 2.5 months, with a median of 2 weeks (15 days). Comparison of diffusion age records with the prehistorical 2.1 ka Moinui and 240 B.P. Hapaimamo Mauna Loa eruptions suggests a decrease in mush disaggregation and mobilisation timescales approaching present time. Although not fully resolved yet, increasing mush disaggregation and mobilisation rates over time could indicate changing eruption priming dynamics. Further diffusion chronometry and geobarometric studies on recent Mauna Loa eruptions are

required to reconcile petrologically constrained magma storage depths and pre-eruptive timescales of magma mobilisation with geophysical models of deep magma storage and transport.

Supplementary Information The online version contains supplementary material available at <https://doi.org/10.1007/s00445-023-01680-x>.

Acknowledgements The entire 1950 AD sample suite was collected by C.R. Thornber and F.A. Trusdell during a field campaign in 2002. We would like to give thanks to John-Wyn Williams (University of Leeds), G.H. Guðfinnsson (University of Iceland), K. Cionoiu, and H.-P. Meyer (Heidelberg University) for sample preparation, polishing, and assistance with EMP analysis. The authors acknowledge editorial handling by A.V. Ivanov and comments by A. Mourey, J. Lubbers, and an anonymous reviewer that substantially improved the manuscript.

Disclaimer Any use of trade, firm, or product names is for descriptive purposes only and does not imply endorsement by the U.S. Government.

Funding Open Access funding enabled and organized by Projekt DEAL. M. Kahl acknowledges funding by the Deutsche Forschungsgemeinschaft (DFG) grants KA 3532/1-1, KA 3532/2-1, and KA 3532/2-2.

Data availability Glass and bulk rock data from the 1950 AD SWRZ eruption of Mauna Loa are also available at Earth Chem (<https://doi.org/10.60520/IEDA/113058>).

Open Access This article is licensed under a Creative Commons Attribution 4.0 International License, which permits use, sharing, adaptation, distribution and reproduction in any medium or format, as long as you give appropriate credit to the original author(s) and the source, provide a link to the Creative Commons licence, and indicate if changes were made. The images or other third party material in this article are included in the article's Creative Commons licence, unless indicated otherwise in a credit line to the material. If material is not included in the article's Creative Commons licence and your intended use is not permitted by statutory regulation or exceeds the permitted use, you will need to obtain permission directly from the copyright holder. To view a copy of this licence, visit <http://creativecommons.org/licenses/by/4.0/>.

References

- Allan ASR, Barker SJ, Millet MA et al (2017) A cascade of magmatic events during the assembly and eruption of a super-sized magma body. *Contrib Mineral Petrol* 172:49. <https://doi.org/10.1007/s00410-017-1367-8>
- Burgisser A, Bergantz G (2011) A rapid mechanism to remobilize and homogenize highly crystalline magma bodies. *Nature* 471:212215. <https://doi.org/10.1038/nature09799>
- Beattie P (1993) Olivine-melt and orthopyroxene-melt equilibria. *Contrib Mineral Petrol* 115:253270. <https://doi.org/10.1007/BF00712982>
- Cashman KV, Blundy JD (2013) Petrological cannibalism: the chemical and textural consequences of incremental magma body growth. *Contrib Mineral Petrol* 166:703–729. <https://doi.org/10.1007/s00410-013-0895-0>
- Chakraborty S (2010) Diffusion coefficients in olivine, wadsleyite and ringwoodite. *Rev Mineral Geochem* 72:603–639. <https://doi.org/10.2138/rmg.2010.72.13>

- Costa F, Chakraborty S (2004) Decadal time gaps between mafic intrusion and silicic eruption obtained from chemical zoning patterns in olivine. *Earth Planet Sci Lett* 227:517–530. <https://doi.org/10.1016/j.epsl.2004.08.011>
- Couperthwaite FK, Morgan DJ, Harvey J, Kahl M (2022) Pre-eruptive timescales from the historical Hapaimamo eruption at Mauna Loa. *J Volcanol Geotherm Res* 432:107690. <https://doi.org/10.1016/j.jvolgeores.2022.107690>
- Couperthwaite FK, Morgan DJ, Pankhurst MJ, Lee PD, Day JMD (2021) Reducing epistemic and model uncertainty in ionic interdiffusion chronology: a 3D observation and dynamic modeling approach using olivine from Piton de la Fournaise, La Réunion. *Am Mineral* 106:481–494. <https://doi.org/10.2138/am-2021-7296CCBY>
- Couperthwaite FK, Thordarson T, Morgan DJ, Harvey J, Wilson M (2020) Diffusion timescales of magmatic processes in the Moinui lava eruption at Mauna Loa, Hawai'i, as inferred from bimodal olivine populations. *J Petrol* 61:egaa058. <https://doi.org/10.1093/petrology/egaa058>
- Davidson JP, Morgan DJ, Charlier BLA, Harlou R, Hora JR (2007) Microsampling and isotopic analysis of igneous rocks: implications for the study of magmatic systems. *Annu Rev Earth Planet Sci* 35:273–311. <https://www.annualreviews.org/doi/full/10.1146/annurev.earth.35.031306.140211>
- Decker RW, Klein FW, Okamura AT, Okubo PG (1995) Forecasting eruptions of Mauna Loa Volcano, Hawai'i. In: Rhodes JM, Lockwood JP (eds) *Mauna Loa revealed: structure, composition, history, and hazards*, vol 92. AGU Monog. <https://doi.org/10.1029/GM092p0337>
- Decker RW, Koyanagi RY, Dvorak JJ, Lockwood JP, Okamura AT, Yamashita KM, Tanigawa WR (1983) Seismicity and surface deformation of Mauna Loa volcano, Hawai'i. *EOS* 64(37):545–547. <https://doi.org/10.1029/EO064i037p00545-01>
- Dohmen R, Becker H-W, Chakraborty S (2007) Fe–Mg diffusion in olivine I: experimental determination between 700 and 1,200°C as a function of composition, crystal orientation and oxygen fugacity. *Phys Chem Miner* 34:389–407. <https://doi.org/10.1007/s00269-007-0157-7>
- Dohmen R, Chakraborty S (2007) Fe–Mg diffusion in olivine II: point defect chemistry, change of diffusion mechanisms and a model for calculation of diffusion coefficients in natural olivine. *Phys Chem Miner* 34:409–430. <https://doi.org/10.1007/s00269-007-0158-6>
- Eggins SM (1992) Petrogenesis of Hawaiian tholeiites: 1, phase equilibria constraints. *Contrib Mineral Petrol* 110:387–397. <https://doi.org/10.1007/BF00310752>
- Finch RH, Macdonald GA (1953) Hawaiian volcanoes during 1950. *USGS Bull* 996-B:49–82
- Finch RH, Macdonald GA (1951) Report of the Hawaiian Volcano Observatory for 1948–49. *USGS Bull* 974-D:103–133
- Gaffney AM (2002) Environments of crystallization and compositional diversity of Mauna Loa xenoliths. *J Petrol* 43:963–981. <https://doi.org/10.1093/petrology/43.6.963>
- Garcia M, Pietruszka AJ, Rhodes JM, Swanson K (2000) Magmatic processes during the prolonged Pu'u 'O'o eruption of Kilauea volcano, Hawai'i. *J Petrol* 41:967–990. <https://doi.org/10.1093/petrology/41.7.967>
- Garcia M (1996) Petrography and olivine and glass chemistry of lavas from the Hawai'i Scientific Drilling Project. *J Geophys Res Solid Earth* 101:11,701–11,713. <https://doi.org/10.1029/95JB03846>
- Garcia M, Hulsebosch TP, Rhodes JM (1995) Olivine-rich submarine basalts from the southwest rift zone of Mauna Loa volcano: implications for magmatic processes and geochemical evolution. In: Rhodes JM, Lockwood JP (eds) *Mauna Loa revealed: structure, composition, history, and hazards*, vol 92. AGU Monog, pp 219–239
- Gerlach TM (1993) Oxygen buffering of Kilauea volcanic gases and the oxygen fugacity of Kilauea basalt. *Geochim Cosmochim Acta* 7:795–814. [https://doi.org/10.1016/0016-7037\(93\)90169-W](https://doi.org/10.1016/0016-7037(93)90169-W)
- Green DH, Ringwood AE (1967) The genesis of basaltic magmas. *Contrib Mineral Petrol* 15:103–190
- Hartley ME, Morgan DJ, Maclennan J, Edmonds M, Thordarson T (2016) Tracking timescales of short-term precursors to large basaltic fissure eruptions through Fe–Mg diffusion in olivine. *Earth Planet Sci Lett* 439:58–70. <https://doi.org/10.1016/j.epsl.2016.01.018>
- Hauri E (2002) SIMS analysis of volatiles in silicate glasses, 2: isotopes and abundances in Hawaiian melt inclusions. *Chem Geol* 183:115–141. [https://doi.org/10.1016/S0009-2541\(01\)00374-6](https://doi.org/10.1016/S0009-2541(01)00374-6)
- Helz RT, Cottrell E, Brounce MN, Kelley KA (2017) Olivine–melt relationships and syneruptive redox variations in the 1959 eruption of Kilauea Volcano as revealed by XANES. *J Volcanol Geotherm Res* 333–334:1–14. <https://doi.org/10.1016/j.jvolgeores.2016.12.006>
- Herzberg C, O'Hara MJ (2002) Plume-associated ultramafic magmas of Phanerozoic age. *J Petrol* 43(10):1857–1883
- Hill DP, Zucca JJ (1987) Geophysical constraints on the structure of Kilauea and Mauna Loa volcanoes and some implications for seismomagmatic processes. In: Decker RW, Wright TL, Stauffer PH (eds) *Volcanism in Hawai'i*. US Geological Survey, Washington, DC, pp 903–917
- Jerram DA, Cheadle MJ, Philpotts AR (2003) Quantifying the building blocks of igneous rocks: are clustered crystal frameworks the foundation? *J Petrol* 44:2033–2051. <https://doi.org/10.1093/petrology/egg069>
- Kahl M, Mutch E, Maclennan J, Morgan DJ, Couperthwaite F, Bali E, Thordarson T, Guðfinnsson GH, Walshaw R, Buisman I, Buhre S, van der Meer QHA, Caracciolo A, Marshall EW, Rasmussen MB, Gallagher CR, Moreland WM, Höskuldsson Á, Askew RA (2022) Deep magma mobilization years before the 2021 CE Fagradalsfjall eruption, Iceland. *Geology* 51(2):184–188. <https://doi.org/10.1130/G50340.1>
- Kahl M, Viccaro M, Ubide T, Morgan DJ, Dingwell DB (2017) A branched magma feeder system during the 1669 eruption of Mt Etna: evidence from a time-integrated study of zoned olivine phenocryst populations. *J Petrol* 58:443–472. <https://doi.org/10.1093/petrology/egi005>
- Kauahikaua JP, Sherrod DR, Cashman KV, Heliker CC, Hon K, Mattox TN, Johnson JA (2003) Hawaiian lava flow dynamics during the Pu'u 'O'o-Kupaianaha eruption; a tale of two decades. In: Heliker C, Swanson DA, Takahashi TJ (eds) *The Pu'u 'O'o-Kupaianaha eruption of Kilauea Volcano, Hawai'i; the first 20 years*, vol 1676. USG Survey Prof Pap, pp 63–87
- Klügel A, Klein F (2006) Complex magma storage and ascent at embryonic submarine volcanoes from the Madeira Archipelago. *Geology* 34:337–340. <https://doi.org/10.1130/G22077.1>
- La Marra D, Poland M, Miklius A, Acocella V (2015) SBAS-InSAR analysis of a decade of surface deformation at Mauna Loa (Hawai'i): preliminary results. In: EGU General Assembly Conference Abstracts, vol 17, p 928
- Lin G, Shearer PM, Matoza RS, Okubo PG, Amelung F (2014) Three-dimensional seismic velocity structure of Mauna Loa and Kilauea volcanoes in Hawai'i from local seismic tomography. *J Geophys Res Solid Earth* 119:4377–4392. <https://doi.org/10.1002/2013JB010820>
- Lipman PW (1995) Declining growth of Mauna Loa during the last 100,00 years: rates of accumulation vs. gravitational subsidence. In: Rhodes JM, Lockwood JP (eds) *Mauna Loa revealed: structure, composition, history, and hazards*, vol 92. AGU Monog, pp 45–80

- Lockwood JP, Dvorak JJ, English TT, Koyanagi RY, Okamura AT, Summers ML, Tanigawa WR (1987) Mauna Loa 1974–1984: a decade of intrusive and extrusive activity. In: Decker RW, Wright TL, Stauffer PH (eds) *Volcanism in Hawai'i*, vol 1350. USGS Survey Prof Pap, pp 537–570
- Lockwood JP, Lipman PW (1987) Holocene eruptive history of Mauna Loa volcano, vol 1350. USGS Prof Pap, pp 509–535
- Lynn KJ, Garcia MO, Shea T, Costa F, Swanson DA (2017) Timescales of mixing and storage for Keanakāko'i Tephra magmas (1500–1820 C.E.), Kīlauea Volcano, Hawai'i. *Contrib Mineral Petrol* 172:76. <https://doi.org/10.1007/s00410-017-1395-4>
- Maaløe S (2004) The PT-phase relations of an MgO-rich Hawaiian tholeiite: the compositions of primary Hawaiian tholeiites. *Contrib Mineral Petrol* 148:236–246. <https://doi.org/10.1007/s00410-004-0601-3>
- Matoza RS, Okubo PG, Shearer PM (2020) Comprehensive high-precision relocation of seismicity on the Island of Hawai'i 1986–2018. *Earth and Space. Science* 7:e2020EA001253. <https://doi.org/10.1029/2020EA001253>
- Matzen AK, Baker MB, Beckett JR, Stolper EM (2011) Fe–Mg partitioning between olivine and high-magnesian melts and the nature of Hawaiian parental liquids. *J Petrol* 52:1243–1263. <https://doi.org/10.1093/petrology/eg055>
- Montierth C, Johnston AD, Cashman KV (1995) An empirical glass-composition-based geothermometer for Mauna Loa lavas. In: Rhodes JM, Lockwood JP (eds) *Mauna Loa revealed: structure, composition, history, and hazards*, vol 92. AGU Monog, pp 207–217. <https://doi.org/10.1029/GM092p0207>
- Moussallam Y, Edmonds M, Scailliet B, Peters N, Gennaro E, Sides I, Oppenheimer C (2016) The impact of degassing on the oxidation state of basaltic magmas: a case study of Kīlauea volcano. *Earth Planet Sci Lett* 450:317–325. <https://doi.org/10.1016/j.epsl.2016.06.031>
- Mourey AJ, Shea T, Hammer JE (2023) Preservation of magma recharge signatures in Kīlauea olivine during protracted storage. *Journal of Geophysical Research: Solid Earth* 128:e2022JB025523. <https://doi.org/10.1029/2022JB025523>
- Nakagawa M, Wada K, Wood P (2002) Mixed magmas, mush chambers and eruption triggers: evidence from zoned clinopyroxene phenocrysts in andesitic scoria from the 1995 eruptions of Ruapehu volcano, New Zealand. *J Petrol* 43:2279–2230. <https://doi.org/10.1093/petrology/43.12.2279>
- Okubo PG, Wolfe CJ (2008) Swarms of similar long-period earthquakes in the mantle beneath Mauna Loa Volcano. *J Volcanol Geotherm Res* 178:787–794. <https://doi.org/10.1016/j.jvolgeores.2008.09.007>
- Okubo PG, Benz HM, Chouet BA (1997) Imaging the crustal magma sources beneath Mauna Loa and Kīlauea volcanoes. Hawai'i. *Geology* 25:867–870. [https://doi.org/10.1130/0091-7613\(1997\)025<0867:ITCMSB>2.3.CO;2](https://doi.org/10.1130/0091-7613(1997)025<0867:ITCMSB>2.3.CO;2)
- Pankhurst MJ, Morgan DJ, Thordarson T, Loughlin SC (2018) Magmatic crystal records in time, space, and process, causatively linked with volcanic unrest. *Earth Planet Sci Lett* 493:231–241. <https://doi.org/10.1016/j.epsl.2018.04.025>
- Park J, Morgan JK, Zelt CA, Okubo PG, Peters L, Benesh N (2007) Comparative velocity structure of active Hawaiian volcanoes from 3-D onshore-offshore seismic tomography. *Earth Planet Sci Lett* 259:500–516. <https://doi.org/10.1016/j.epsl.2007.05.008>
- Poland MP, Miklius A, Montgomery-Brown EK (2014) Magma supply, storage, and transport at shield-stage Hawaiian volcanoes, vol 1801. USGS Prof Pap, pp 1–52
- Prior DJ, Boyle AP, Brenker F, Cheadle MC, Day A, Lopez G, Peruzzi L, Potts G, Reddy S, Spiess R, Timms NE (1999) The application of electron backscatter diffraction and orientation contrast imaging in the SEM to textural problems in rocks. *Am Mineral* 84:1741–1759. <https://doi.org/10.2138/am-1999-11-1204>
- Putirka KD (2008) Thermometers and barometers for volcanic systems. *Rev Mineral Geochem* 69:61–120. <https://doi.org/10.2138/rmg.2008.69.3>
- Roeder PL, Emslie RF (1970) Olivine-liquid equilibrium. *Contrib Mineral Petrol* 29:275–289
- Rhodes JM (1995) The 1852 and 1868 Mauna Loa picrite eruptions: clues to parental magma compositions and the magmatic plumbing system. In: Rhodes JM, Lockwood JP (eds) *Mauna Loa revealed: structure, composition, history, and hazards*, vol 92. AGU Monog, pp 241–262. <https://doi.org/10.1029/GM092p0241>
- Rhodes JM (1988) Geochemistry of the 1984 Mauna Loa eruption: implications for magma storage and supply. *J Geophys Res Solid Earth* 93(B5):4453–4466. <https://doi.org/10.1029/JB093iB05p04453>
- Schleicher JM (2017) Crystal-scale control on magmatic mush mobilization and mixing. PhD thesis, University of Washington, USA
- Shea T, Matzen AK, Mourey AJ (2022) Experimental study of Fe–Mg partitioning and zoning during rapid growth of olivine in Hawaiian tholeiites. *Contrib Mineral Petrol* 177:114. <https://doi.org/10.1007/s00410-022-01969-8>
- Streck MJ (2008) Mineral textures and zoning as evidence for open system processes. *Rev Mineral Geochem* 69:595–622. <https://doi.org/10.2138/rmg.2008.69.15>
- Stroncik NA, Klügel A, Hansteen TH (2009) The magmatic plumbing system beneath El Hierro (Canary Islands): constraints from phenocrysts and naturally quenched basaltic glasses in submarine rocks. *Contrib Mineral Petrol* 157:593–607. <https://doi.org/10.1007/s00410-008-0354-5>
- Taggart JE, Lindsay JR, Scott BA, Vivit DV, Bartel AJ, Stewart KC (1987) Analysis of geological materials by wavelength-dispersive X-ray fluorescence spectrometry. In: Baedecker PH (ed) *Methods for geochemical analysis*, vol 1170. USGS Bull, pp E1–E19
- Thomson A, MacLennan J (2013) The distribution of olivine compositions in Icelandic basalts and picrites. *J Petrol* 54:745–768. <https://doi.org/10.1093/petrology/egs083>
- Thorner CR (2001) Olivine-liquid relations of lava erupted by Kīlauea volcano from 1994–1998: Implications for shallow magmatic processes associated with the ongoing east rift zone eruption. In: Canil D, Jamieson H, Martin R (eds) *Phase equilibria in basaltic systems*, vol 39. *Canadian Mineralogist*, pp 239–266. <https://doi.org/10.2113/gscanmin.39.2.239>
- Thorner CR, Sherrod DR, Siems DF, Heliker CC, Meeker GP, Oscarson RL, Kauahikaua JP (2002) Whole-rock and glass major-element geochemistry of Kīlauea Volcano, Hawai'i, near-vent eruptive products: September 1994 through September 2001. USGS Open File Rep 02-17: 41.
- Thorner CR, Heliker CC, Sherrod DR, Kauahikaua JP, Miklius A, Okubo PG, Trusdell FA, Budahn JR, Ridley WI, Meeker GP (2003) Kīlauea east rift zone magmatism: an episode 54 perspective. *J Petrol* 44:1525–1559. <https://doi.org/10.1093/petrology/egg048>
- Thorner CR, Trusdell FA (2008) Field, petrologic and experimental evidence for rapid transport of large magma volumes from great depths during the 1950 eruption of Mauna Loa, Hawai'i. IAVCEI General Assembly, Reykjavik, Iceland
- Trusdell FA (1995) Lava flow hazards and risk assessment on Mauna Loa volcano, Hawai'i. In: Rhodes JM, Lockwood JP (eds) *Mauna Loa revealed: structure, composition, history, and hazards*, vol 92. AGU Monog, pp 327–336. <https://doi.org/10.1029/GM092p0327>
- Trusdell FA (2012) Mauna Loa – history, hazards, and risk of living with the world's largest volcano, vol 3104. USGS Fact Sheet
- Wanless VD, Garcia MO, Rhodes JM, Weis D, Norman MD (2006) Shield-stage alkalic volcanism on Mauna Loa Volcano, Hawai'i.

- J Volcanol Geotherm Res 151:141–155. <https://doi.org/10.1016/j.jvolgeores.2005.07.027>
- Wieser PE, Gleeson M, Matthews S, DeVitre CL, Gazelet E (2023) Determining the pressure – temperature – composition (P-T-X) conditions of magma storage. In: In press with Treatise on geochemistry. <https://doi.org/10.31223/X50M44>
- Wieser PE, Kent AJR, Till CB, Donovan J, Neave DA, Blatter DL, Krawczynski MJ (2022) Barometers behaving badly I : assessing the influence of analytical and experimental uncertainty on clinopyroxene thermobarometry calculations at crustal conditions. *J Petrol* 64:egac126. <https://doi.org/10.1093/petrology/egac126>
- Wieser PE, Lamadrid H, Maclennan J, Edmonds M, Matthews S, Iacovino K, Jenner FE, Gansecki C, Trusdell F, Lee RL, Ilyinskaya E (2021) Reconstructing magma storage depths for the 2018 Kīlauean eruption from melt inclusion CO₂ contents: the importance of vapor bubbles. *Geochem Geophys Geosyst* 22:e2020GC009364. <https://doi.org/10.1029/2020GC009364>
- Wilding JD, Zhu W, Ross ZE, Jackson JM (2023) The magmatic web beneath Hawai‘i. *Science* 379:462–468. <https://doi.org/10.1126/science.ade5755>
- Wyss M, Koyanagi RY (1992) Isoleismal maps, macroseismic epicenters and estimated magnitudes of historic earthquakes in the Hawaiian Islands, vol 2006. USGS Bull, p 93